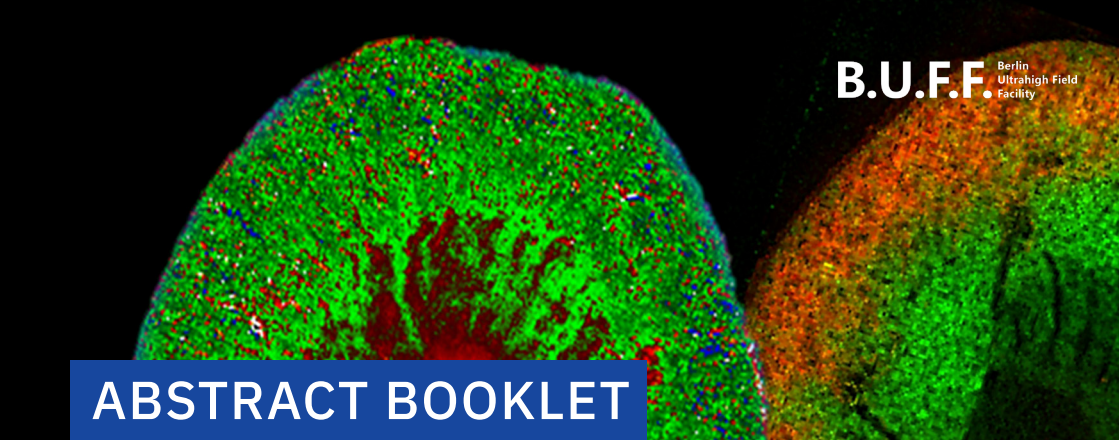

B.U.F.F. Berlin Ultrahigh Field Facility

ABSTRACT BOOKLET

16. ANNUAL SCIENTIFIC SYMPOSIUM

Ultrahigh Field Magnetic Resonance: Clinical Needs, Research Promises and Technical Solutions

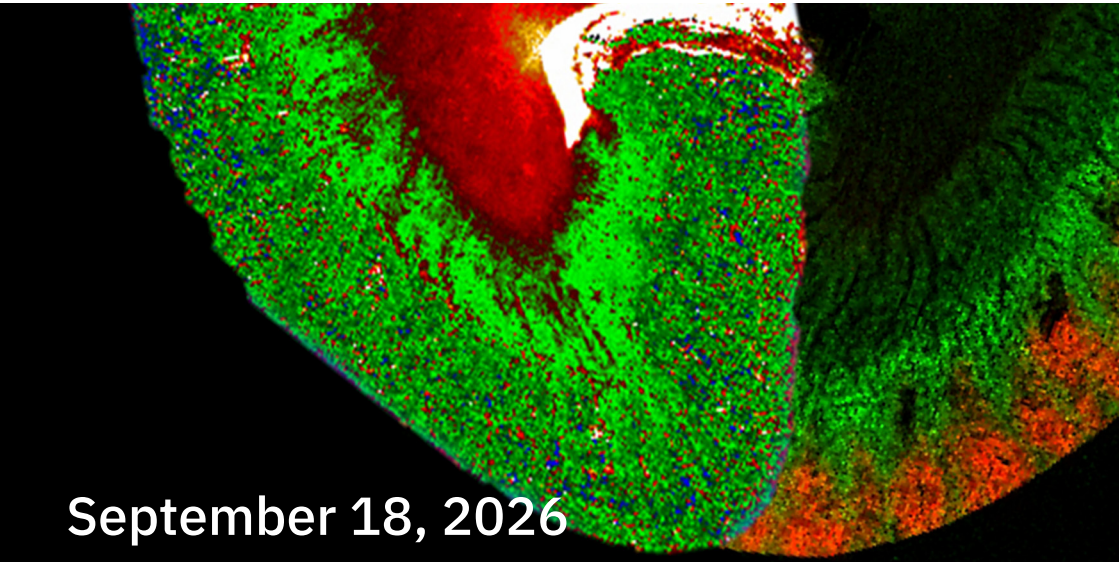

September 18, 2026

9:00 am - 6:30 pm

Max Delbrück Communications Center (MDC.C)

MAX DELBRÜCK CENTER

www.mdc-berlin.de

www.mdc-berlin.de/MR_Symposium_2026

Max Delbrück Center for Molecular Medicine
in the Helmholtz Association

Robert-Rössle-Straße 10, 13125 Berlin, Germany

Message from the organizers

Dear colleagues and friends,

Very warm welcome to Berlin. It is time to ride the wave of ultrahigh field MRI again.

We are most of all excited by the larger audience that has joined us for the **16th Scientific Symposium on Clinical Needs, Research Promises and Technical Solutions in Ultrahigh Field Magnetic Resonance**.

Imaging provides a unique bridge across scales and time in life science and medicine—from molecular and cellular processes to whole-body function, and from ultrafast biological events to long-term population studies. By combining imaging with data science, we can transform complex observations into a more integrated understanding of tissues, organs, and organisms, enabling earlier disease detection and intervention.

Magnetic resonance has evolved rapidly over the past decades, enabling an expanding range of applications in basic, translational and clinical research. At the same time, increasingly complex and high-dimensional imaging datasets have made data science indispensable to modern MRI research. Artificial intelligence (AI) is now transforming image reconstruction, acquisition, automated analysis, quantitative biomarker development and the integration of imaging with clinical and molecular data.

These advances offer new opportunities for earlier disease detection, improved patient stratification, and more precise monitoring of disease progression and treatment response. Advancing this field requires interdisciplinary collaboration, international partnerships, and a shared vision that connects technology, biological understanding, and clinical impact.

The symposium brings together life scientists, engineers, data scientists and clinicians at all career stages, from students and trainees to advanced users, or technical experts to discuss current clinical needs, emerging research opportunities and innovative technical solutions in MRI. It is a platform for interdisciplinary exchange, new collaborations and discussion of how data science and AI can help shape the future of imaging research.

We very warm welcome you to Berlin and to ultrahigh field MR.

Grant Support

The organizers wish to acknowledge the generous support provided by the Deutsche Forschungsgemeinschaft (DFG), the German Research Foundation

About the DFG:

"The DFG is the self-governing organization for science and research in Germany. It serves all branches of science and the humanities. In organizational terms, the DFG is an association under private law. Its membership consists of German research universities, non-university research institutions, scientific associations and the Academies of Science and the Humanities.

The DFG supports projects from all scientific subject areas and especially promotes interdisciplinary cooperation between researchers. DFG funding enables cooperation between researchers from all branches of the science system as well as the formation of internationally conspicuous priorities at universities and non-university research institutions.

The foundation actively encourages international research cooperation: all of its programmes promote cooperation between scientists and academics in Germany and their colleagues abroad. It places special emphasis on collaboration in the scientific community in the European Research Area.

The DFG funds knowledge-oriented research and it welcomes and supports the cooperation of science with those who apply science in all areas of social life. This includes the interaction of scientific findings with industry and institutions like museums, academies of music, hospitals, and in public-private partnerships. Science and research are by definition international. Thus, the DFG's statutes include an obligation to foster contacts between scientists and researchers in Germany and abroad.

To advance internationalization, the DFG has opened its funding programmes for international collaboration between researchers – an absolute necessity for Germany in its role as a pioneering and simultaneously cosmopolitan centre of research and science."

Funded by
DFG Deutsche Forschungsgemeinschaft
German Research Foundation

For further details please visit: **www.dfg.de/en**

Table of Contents

Organization

ORGANIZERS:

Thoralf Niendorf
MDC & Charité, Berlin

Lucio Frydman
Weizmann Institute of Science, Rehovot, Israel

Christoph Lippert
HPI, Potsdam

Michal Neeman
Weizmann Institute of Science, Rehovot, Israel

Sonia Waiczies
MDC, Berlin

Min-Chi Ku
MDC, Berlin

CONFERENCE OFFICE:

Carolin Bechtloff

Max Delbrück Center for Molecular Medicine in the Helmholtz Association
Robert-Rössle-Strasse 10
13125 Berlin

E-Mail: MRSymposium@mdc-berlin.de
Phone: + 49 30 9406 3978

16TH ANNUAL SCIENTIFIC SYMPOSIUM ON ULTRAHIGH FIELD MAGNETIC RESONANCE

Friday, 18th September 2026

09:00	**WELCOME** chair: Thoralf Niendorf, Berlin, Germany Min-Chi Ku, Berlin, Germany
09:10	KEYNOTE LECTURE **Seeing the Unseen: Magnetic Resonance Imaging at 10.5 T** Kamil Ugurbil, University of Minnesota, Minneapolis, USA

SCIENTIFIC SESSION I

GETTING TO THE MATTER OF THE HEART: CLINICAL NEEDS AND RESEARCH PROMISES OF CARDIOVASCULAR AND BODY UHF-MR

chair: Jutta Ellermann, Minneapolis, USA
Min-Chi Ku, Berlin, Germany

09:40	**Taking the Strain: Bridging Preclinical and Clinical Insights in Hypertrophic Cardiomyopathy** Siqin Liu, Max Delbrück Center, Berlin, Germany
10:00	**UHF Clinical Imaging Outside the Brain with 5T MRI** Yongquan Ye, MR R&C United Imaging Healthcare Europe
10:20	**Insights from the German National Cohort: Native T1 Mapping of the Heart Reveals Associations with Sex, Age and Cardiometabolic Risk Factors** Clemens Ammann, Charité-Universitätsmedizin, Berlin, Germany
10:40	**Magnetic Resonance Spectroscopy Applications in Diabetes Research** Vera Schrauwen-Hinderling, German Diabetes Center (DDZ), Düsseldorf, Germany

Program September 18, 2026

11:00	**POSTER POWER SESSION (3 x 3 min)** **Uncovering Energetic Remodeling in Genetic Heart Disease by ^{31}P MRS** Yingke Hou, Max Delbrück Center, Berlin, Germany **Cardiac Phase-Resolved T_1 and T_2 * relaxometry in Murine Hearts** Shahriar Shalikar, Max Delbrück Center, Berlin, Germany **Multiparametric CMR Reveals Early Myocardial Perfusion Deficits Alongside Alterations in Diastolic Function in Hypertrophic Cardiomyopathy** Xiaomin Wang, Max Delbrück Center Berlin, Germany
11:10	**PANEL DISCUSSION: CARDIAC AND BODY MRI at UHF**
11:25	**COFFEE BREAK / RELAXATION WITH LIVE MUSIC**

SCIENTIFIC SESSION II

GETTING TO THE MATTER OF THE BRAIN: CLINCIAL NEEDS AND RESEARCH PROMISES FOR NEUROVASCULAR UHF-MR AND RELATED FIELDS

chair: Wulf-Ingo Jung, Ettlingen, Germany
Sonia Waiczies, Berlin, Germany

11:45	**Looking for Central Vein Signs: Simultaneous T2, T2*, and R2′ Mapping for Multiple Sclerosis Using Nonlinear Model-Based Reconstruction** Jose Raul Velasquez Vides, Max Delbrück Center, Berlin, Germany
12:05	**Artificial Intelligence in Brain MRI: Insights into Depression, Anxiety, and Alcohol Use from the German National Cohort** Julius Wiegert, Central Institute of Mental Health, Mannheim, Germany
12:25	**Hot, Cold, and BOLD fMRI at 7.0 T: Thermal Signal Processing in the Insular Cortex Follows Architectural Principles** Henning Reimann, Northeastern University/Athinoula A. Martinos Center, MGH, Boston, MA, USA
12:45	**Living cortical organoids at 28.2 T MRI: a new frontier for microstructural MRI** Tatiana Nikolaeva, University Medical Center Utrecht, The Netherlands

13:05	**POSTER POWER SESSION (4 x 3 min)** **Can Large Language Models Reason Through MRI Physics? A Simulation-Based Framework for Evaluating MRI Acquisition Parameter Interpretation** Muna AlMulla, Kuwait University, Kuwait, Kuwait **Metamaterial-integrated bow-tie antenna array for magnetic field shaping at 7T: a route towards RF phase-encoded B1 and SAR steering** Jegyasu Gupta, Max Delbrück Center, Berlin, Germany **Evaluation of Image Contrast-Agnostic Brain MRI Segmentation on Heterogeneous Clinical Data** Jason Millward, Max Delbrück Center, Berlin, Germany **Silicon Integrated RF Electronics for Low-Noise Multichannel UHF MRI** Christof Pfannenmüller, Otto-von-Guericke-Universität Magdeburg, Magdeburg, Germany
13:20	**PANEL DISCUSSION: BRAIN MRI at UHF**
13:35	**LUNCH BREAK**

SCIENTIFIC SESSION III

TRANSLATIONAL RESEARCH: FROM BLUE SKY EXPLORATIONS EN ROUTE TO CLINICAL APPLICATIONS

chair: Vera Schrauwen-Hinderling, Düsseldorf, Germany
Philipp Boehm-Sturm, Berlin, Germany

14:15	KEYNOTE LECTURE **k-Space Encounters – Where Art & Science Become MRI Techno** Johanna Barnbeck, Spread the Nerd, Berlin, Germany
14:35	**Why We Still Need More Tesla: UHF MRI as a Platform for New Insights into Biology** Wulf-Ingo Jung, Bruker Biospin MRI GmbH, Ettlingen, Germany
14:55	**Unmasking Brain Fluid Dynamics under Awake Conditions: The Path to Translation** Ryszard Gomółka, University of Copenhagen, Denmark

Program September 18, 2026

15:15	**Integrative Ecophysiology: MRI and MRS in View of Climate Change** Christian Bock, Alfred Wegener Institute, Bremerhaven, Germany
15:35	**Guardian of the Body's Inner Ocean: Probing the Tubule System with Quantitative MRI from Experimental Models to Humans** Thomas Gladytz, Max Delbrück Center, Berlin, Germany
15:55	**POSTER POWER SESSION (1 x 3 min)** **Fluorine MR relaxation properties of fluorinated bioisosteres of evobrutinib** Lison Guillaume, Max Delbrück Center, Berlin, Germany
16:00	**PANEL DISCUSSION: TRANSLATIONAL MRI at UHF**
16:15	**COFFEE BREAK / RELAXATION WITH LIVE MUSIC**

SCIENTIFIC SESSION IV
LOOKING AT THE HORIZON

chair: Mikolaj Pawlak, Poznan, Poland
Jason Millward, Berlin, Germany

16:35	**The Invisible Heat, Revealed: Ultrafast MR Thermometry for Monitoring of Thermal Therapy** Bruno Quesson, University of Bordeaux, France
16:55	**Beyond: Metamaterial Antennas Enhance MRI of the Eye and Brain at 7.0 T** Thoralf Niendorf, Max Delbrück Center, Berlin, Germany
17:15	**From Physics to Learning: Trustworthy AI as a bridge in Quantitative MRI** Xinqi Li, Max Delbrück Center, Berlin, Germany
17:35	**MAGNETOM Terra.X: Progress in Clinical Ultralight Field MRI at 7.0 T** Jan Ruff, Siemens Healthineers, Erlangen, Germany
17:55	**PANEL DISCUSSION: FUTURE of UHF MRI**
	Awards & Adjourn

Speaker Abstracts

(In order of the talks in the program schedule)

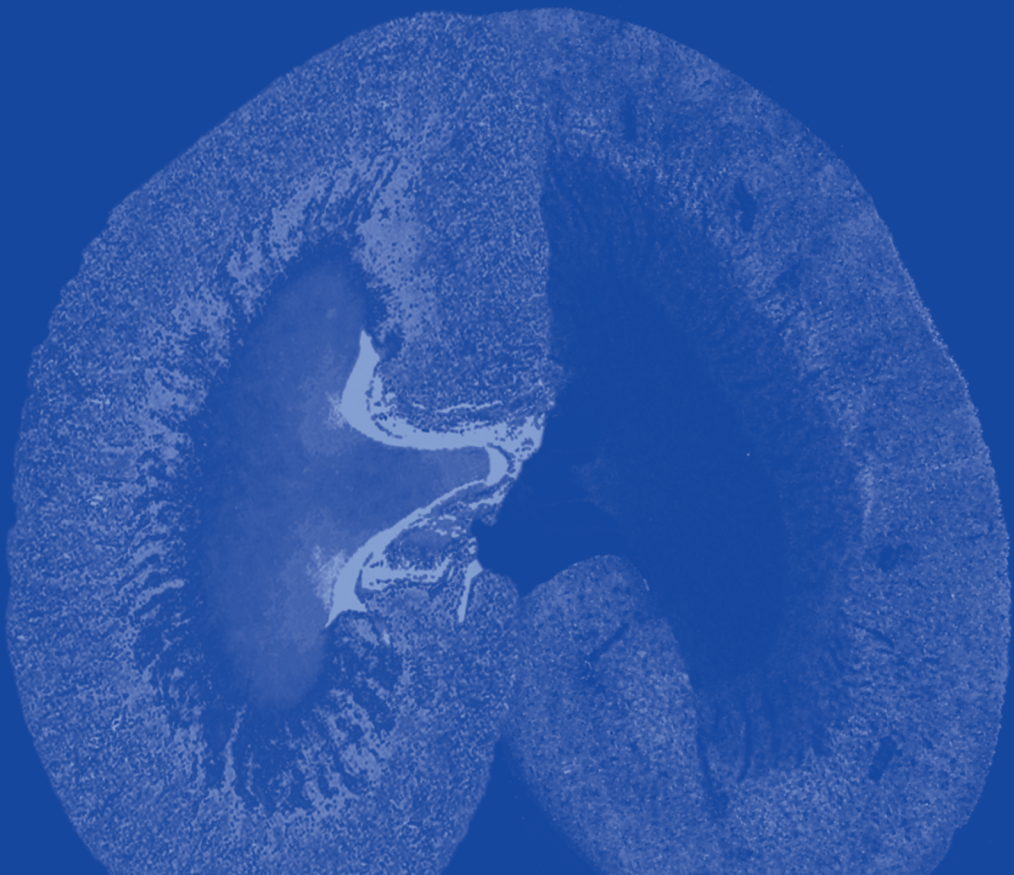

T1

Seeing the Unseen: Magnetic Resonance Imaging at 10.5 T

Kamil Ugurbil[1]

[1]*University of Minnesota, Minneapolis, USA*

Scientific advances strongly rely on development of new and novel tools that expand experimental capabilities and enable the acquisition of previously unavailable information. This is certainly the case for the efforts targeting the understanding of brain function in biological terms, and deciphering the perturbations that underlie neurodegenerative and neuropsychiatric disorders. Cognizant of the sensitivity and resolution challenges needed to cover the vast spatial scales over which the brain operates, our primary focus has been to develop instrumentation and techniques for imaging at high magnetic fields first focusing on developing 7 Tesla and more recently, on pushing the ultrahigh field boundary above 10 Tesla, specifically10.5T. We have recently demonstrated major gains in SNR, anatomical imaging, and BOLD contrast for functional imaging at 10.5T and utilized these gains to achieve functional imaging in the human brain that has been difficult to realize at 7T. These results will be reviewed and covered in this lecture.

T2

Taking the Strain: Bridging Preclinical and Clinical Insights in Hypertrophic Cardiomyopathy

Siqin Liu[1]

[1] *Max Delbrück Center for Molecular Medicine, Berlin, Germany*

Early myocardial dysfunction in hypertrophic cardiomyopathy (HCM) can remain invisible to conventional measures, creating a need for sensitive markers of subclinical disease. Cardiac magnetic resonance feature tracking (CMR-FT) may provide such a window into early myocardial dysfunction—but can this approach be translated to ultrahigh-field 7 T CMR?

In a knock-in HCM mouse model carrying a Mybpc3 mutation, we found that left- and right-ventricular longitudinal strain and LV torsion were impaired before conventional measures of cardiac function showed abnormalities.

These changes were associated with mitochondrial remodeling and were particularly pronounced in females, linking altered myocardial mechanics to early disease biology.

We then translated CMR-FT to human 7 T CMR and benchmarked it against clinical 3 T imaging in healthy participants and patients with HCM. Standard 7 T acquisitions showed reduced discrimination between healthy and HCM myocardium, revealing a key technical barrier: limited signal-to-noise ratio and blood–myocardium contrast compromised strain assessment. To overcome this, we developed a systematic acquisition framework combining quantitative $B1^+$ mapping with excitation flip-angle optimization. This approach improved image quality and strain quantification, while establishing a reproducible relationship between transmit reference voltage, $B1^+$, and the achieved flip angle.

From detecting early mechanical dysfunction in a preclinical model to overcoming the technical barriers of human 7 T CMR, this work establishes a translational pathway toward more sensitive quantitative phenotyping of HCM.

T3

UHF Clinical Imaging Outside the Brain with 5T MRI

Yongquan Ye[1]

[1]*MR R&C, United Imaging Healthcare Europe*

There are major trends in UHF on developing clinical potentials, where more fundamental challenges arise over non-neuro scans. With the newly emerged 5T system passing all major regulations for whole body clinical imaging, a wide range of clinical experience with UHF MRI outside the brain has fastly emerged, spanning cardiac, abdominal, musculoskeletal, and pelvic applications. Higher signal enables improved spatial resolution and accelerated acquisitions, while B1 inhomogeneity, RF safety, hardware supports and clinically oriented workflows at 5T become technically manageable via tailored hardware and software ecosystems. Clinical evidence has demonstrated diagnostic quality comparable or superior to 3T from head to toe, positioning 5T as a promising platform for routine clinical UHF body imaging.

T4

Insights from the German National Cohort: Native T1 Mapping of the Heart Reveals Associations with Sex, Age and Cardiometabolic Risk Factors

Clemens Ammann[1]

[1]*Charité – Universitätsmedizin, Berlin, Germany*

Myocardial native T1 mapping enables quantitative, non-invasive tissue characterization and may detect subclinical changes in myocardial structure and composition. We investigated how age, sex, and cardiometabolic risk factors are associated with myocardial T1 as a potential imaging marker of myocardial target-organ involvement. To this end, we analyzed 29,573 participants of the German National Cohort (NAKO) who underwent midventricular T1 mapping at 3.0T along with deep clinical phenotyping. Artificial intelligence-assisted myocardial segmentation was followed by manual quality control. Associations of cardiometabolic risk factors with myocardial T1 were evaluated using multiple linear regression models adjusted for age, sex, heart rate, imaging site, and comorbidities. After quality control, 27,794 participants (12,401 women; 20–75 years) were included. Mean T1 was higher in women (1,231 ± 33 ms) than in men (1,209 ± 34 ms), with the sex difference gradually declining with age. In adjusted analyses, T1 was significantly elevated in individuals with diabetes, kidney disease, and current smoking. Conversely, hyperlipidemia was significantly associated with lower T1, warranting further investigation of potential direct effects of blood lipids on the heart. Associations with hypertension showed sex-specific patterns: women had lower T1 values, while T1 increased with hypertension severity in men. Overall, these findings demonstrate that myocardial native T1 varies by sex and age and shows distinct sex-specific associations with major cardiometabolic risk factors, supporting its role as a sensitive imaging marker of subtle myocardial alterations.

T5

Magnetic Resonance Spectroscopy Applications in Diabetes Research

Vera Schrauwen-Hinderling[1]

[1]*German Diabetes Center (DDZ), Düsseldorf, Germany*

Magnetic Resonance Spectroscopy (MRS) offers unique possibilities to investigate metabolism in vivo. Many chronic diseases are characterized by a mismatch between high substrate availability (with increased lipid and glycogen stores) and insufficient oxidative capacity. Indeed, increased adipose tissue volume, increased lipid storage in the liver, skeletal muscle, myocardium was shown to correlate strongly with insulin resistance, an early hallmark in the development of type 2 diabetes mellitus and other chronic metabolic diseases. At the same time, impaired mitochondrial function (reduced oxidative capacity) was reported in these organs. Multinuclear (1H-, 13C-, 31P-) MRS makes it possible to investigate both sides of the balance and to monitor interventions targeting improvements in metabolic health. Methodological improvements and newly designed MRS sequences can also specifically target metabolites that are not directly visible in the spectrum and open avenues to gain even more non-invasive information that was not accessible to date. In this way, for example fatty acid composition in the liver, as well as acetylcarnitine and NAD+/NADH in skeletal muscle were shown to be quantifiable in vivo and of physiological relevance.

T6

Looking for Central Vein Signs: Simultaneous T2, T2*, and R2′ Mapping for Multiple Sclerosis Using Nonlinear Model-Based Reconstruction

Jose Raul Velasquez Vides[1]

[1]*Max Delbrück Center for Molecular Medicine, Berlin, Germany*

The central vein sign (CVS), a thin vein running through the center of a white matter lesion best seen on T2*-weighted imaging, has emerged as a promising MRI biomarker for distinguishing multiple sclerosis (MS) from other white matter lesion mimics. However, robust CVS assessment together with T2 and R2′ mapping typically requires long, separately acquired scans, limiting clinical feasibility.

We present 2in1-RARE-EPI, an acquisition combining a RARE module with an EPI module to jointly encode T2 and T2* information, paired with nonlinear model-based reconstruction that estimates T2, T2*, and R2′ maps directly from undersampled radial k-space data. This synergy enables simultaneous, co-registered T2/T2*/R2′ mapping with a 7.5-fold scan-time reduction relative to reference multiecho spin-echo and multiecho gradient-echo methods.

We validated the approach in a phantom, healthy subjects, and MS patients, showing close agreement with reference T2 and T2* maps. At higher acceleration factors, nonlinear model-based reconstruction preserved spatial detail and accuracy more consistently than parallel imaging compressed sensing (PICS). In MS patients, the method detected small focal lesions across all three parametric maps and enabled visualization of the central vein sign.

Scan time reduction facilitated by nonlinear model-based reconstruction of 2in1-RARE-EPI provides a technical foundation for enhanced patient compliance, and is a fundamental precursor for broader clinical studies on the potential of T2, T2*, and R2′ as imaging biomarkers.

T7

Artificial Intelligence in Brain MRI: Insights into Depression, Anxiety, and Alcohol Use from the German National Cohort

Julius Wiegert[1]

[1]*Central Institute of Mental Health, Mannheim, Germany*

Large imaging cohorts combined with AI now make it possible to map continuous brain variation, define normative reference spaces, and test whether subtle brain–phenotype relationships generalize across cohorts. This talk illustrates these opportunities through two complementary studies using structural MRI from the German National Cohort (NAKO), with a focus on depression, anxiety, and alcohol use.

Self-supervised learning was used to derive data-driven representations of distributed brain structure at population scale. These representations enabled two complementary analyses: one examined how individuals with depressive, anxiety, and alcohol-related symptoms deviate from normative population variation, while the other identified continuous structural brain axes associated with symptom severity. Depression and anxiety showed overlapping patterns of brain-structural deviation, alcohol-related variation was more distinct and generally more robust. Several findings generalized beyond the NAKO to independent samples, including the UK Biobank, and also converged with clinical diagnosis, peripheral biomarkers, and cognitive performance.

Together, these studies show what becomes possible when neuroimaging moves to population scale: subtle distributed effects can be detected, quantified relative to normative variability, compared across phenotypes, and tested for reproducibility and external validity. At the same time, the findings underscore that these signals are currently more informative for understanding population-level neurobiological dimensions than for individual diagnosis. AI applied to large-scale MRI may therefore be most powerful not as a diagnostic shortcut, but as a tool for charting the structure of brain variation across the population.

T8

Hot, Cold, and BOLD fMRI at 7.0 T: Thermal Signal Processing in the Insular Cortex Follows Architectural Principles

Henning Reimann[1]

[1]*Northeastern University/Athinoula A. Martinos Center, MGH, Boston, MA, USA*

Why does cold move us, and warmth invite us to stay? The cerebral cortex converts sensory signals into motor responses — behavior that acts on the world and visceromotor commands to keep the body ahead of its needs — a predictive regulatory principle called allostasis. This signal conversion runs along cortical architecture, from granular sensory, through limbic dysgranular, to agranular motor-control cortices. The insula performs it most compactly. As the primary interoceptive cortex, it translates bodily signals directly and alone spans the granular-to-agranular gradient — a miniature cortex for studying the allostatic principle. Yet how the human insula turns temperature into thermoregulation, and whether this conversion occurs there at all, remains unknown. Here, we test both using 7 T fMRI at 1.5 mm in individual subjects.

To map thermal responses across insular subdivisions, we employed spatially adaptive smoothing and controlled the false-positive rate in single subjects. Hot and cold signals from the skin travel in afferents at different speeds (fast Aδ- and slow C-fibers), and a single hemodynamic model conflates them, which demands modeling each condition separately.

We identified a primary thermal cortex at the posterodorsal granular operculo-insular interface and tracked signal propagation to anteroventral agranular motor-control regions by exploiting dynamic functional connectivity at high temporal resolution from two-TR response vectors within the general linear model. Both functional connectivity and diffusion tractography linked these anterior insular fields to visceromotor and skeletomotor centers of thermoregulation — the parabrachial nucleus and hypothalamus.

These results provide the first structural and functional evidence that thermoreception and thermoregulation converge in the human insula, along the cytoarchitectonic gradient that compresses sensory signals into bodily control.

T9

Living cortical organoids at 28.2 T MRI: a new frontier for microstructural MRI

Tatiana Nikolaeva[1]

[1]*University Medical Center Utrecht, The Netherlands*

Quantitative microstructural magnetic resonance imaging (MRI) can noninvasively probe tissue organization at micrometer scales. However, its translation toward clinical applications is limited by challenges in validation and optimization using human-relevant models. Organoids provide unique models of human tissue development and organization, yet methods for non-destructive, longitudinal assessment of their microstructure are lacking. This talk will focus on the potential of ultra-high-field MRI at 28.2 T for imaging living cortical organoids, combined with 3D lightsheet (LS) microscopy for microstructural validation.

Focusing on cortical organoids, We show longitudinal experiments to assess structural changes, extended microstructural MRI experiments to characterize differences between young and mature organoids, and microstructural tensor imaging with spatial resolutions down to $(20\ \mu m)^3$, with adequate signal-to-noise ratio and feasible scan times. We further discuss the extension of this microstructural MRI workflow to other organoid models, including colorectal and kidney organoids.

T10

k-Space Encounters: Where Art and Science Becomes MRI Techno

Johanna Barnbeck[1]

[1]*Spread the Nerd, Berlin, Germany*

Magnetic Resonance Imaging (MRI) is one of the most advanced technologies in medicine and biomedical research, yet its complexity often limits public engagemennt. MRI Techno explores how artistic practice can create new ways of experiencing and understanding MRI by transforming the sounds generated during imaging into music, audiovisual works, and participatory formats.

At the core of the MRI Techno project lies an open source sound library and transdisciplinary collaboration between MRI researchers, patients, artists, musicians, and science communicators. The project treats MRI not only as a scientific instrument, but also as a cultural, sensory, and creative medium. By working with the acoustic signatures of MRI sequences, MRI Techno opens alternative entry points to conversations about imaging technologies, health, and research.

This presentation introduces the project's concept, collaborative methodology, and early outcomes, highlighting how art-science partnerships can foster curiosity, accessibility, and public dialogue around advanced MRI technologies.

T11

Why We Still Need More Tesla: UHF MRI as a Platform for New Insights into Biology

Wulf-Ingo Jung[1]

[1]*Bruker Biospin MRI GmbH, Ettlingen, Germany*

Ultra-high-field (UHF) MRI delivers far more than improved image quality. By increasing sensitivity, spatial resolution, spectral separation, susceptibility contrast, and multinuclear imaging performance, UHF MRI enables researchers to investigate biological structure, function, and metabolism with unprecedented detail. These capabilities support the visualization of tissue microstructure, improved localization of neuronal activity, enhanced metabolite detection, and quantitative assessment of biological processes that are difficult or impossible to study at lower field strengths.

Recent advances in high-performance gradients, RF technology, CryoProbe detection, AI-assisted image reconstruction, and hyperpolarized metabolic imaging are further expanding the scientific reach of UHF MRI. Together, these innovations enable highly sensitive anatomical, functional, and metabolic investigations across neuroscience, oncology, metabolic research, and drug discovery, while helping bridge the gap between preclinical research and clinical translation.

Using selected examples from recent preclinical research, this presentation will illustrate how UHF MRI is evolving from a high-resolution imaging modality into a comprehensive platform for functional, metabolic, and molecular phenotyping, enabling new discoveries and shaping the future of translational imaging.

T12

Unmasking Brain Fluid Dynamics under Awake Conditions: The Path to Translation

Ryszard Gomółka[1]

[1]*University of Copenhagen, Denmark*

Diffusion-weighted imaging (DWI) has increasingly been proposed for non-invasive evaluation of glymphatic transport and interstitial fluid (ISF) dynamics [1–3]. Thus, using multimodal in vivo MRI in ketamine/xylazine anesthetized mice, we first examined the impact of genetic aquaporin-4 (AQP4) deletion on brain water mobility [2]. Compared to wildtype littermates, AQP4-deficient mice showed increased slow MR diffusivities coinciding with reduced MR tracer clearance, larger brain volumes, and reduced CSF/brain volume ratio, indicating brain-wide interstitial fluid stagnation. We next verified DWI's sensitivity to AQP4-dependent water changes pharmacologically [4]. The AQP4 blocker AER-271 prevented the rise in slow MR diffusivities seen in WT mice, attributed to ISF-space changes, paralleling inhibited glymphatic influx/efflux on independent assays. However, these and most preclinical glymphatic MRI investigations are performed under anesthesia, which alters cardiorespiratory function, perfusion, oxygenation, and brain water dynamics relative to wakefulness [5–8]. When comparing different anesthetics, it remains unclear whether DWI-derived markers reflect ISF-space properties or state-dependent perfusion effects. Thus, we combined standard and spectral DWI/IVIM with MR tracer dynamics, physiological monitoring, and perfusion imaging (laser-Doppler, μCT) in mice imaged awake and under isoflurane or ketamine/xylazine anesthesia. Both anesthetics altered ISF- and microvascular-related spectral MR diffusivity components relative to the awake state, with divergent and oppositely directed effects on slow and fast diffusivities. These shifts did not correlate with MR tracer-derived glymphatic influx, but tracked anesthetic-specific physiological signatures (heart rate, respiratory rate, capillary transit time), concluding that rodent glymphatic imaging should be performed in a single state, with awake conditions offering the highest translational relevance.

References

[1] Urushihata, T., et al. Eur Radiol Exp, 2021. **5**(1): p. 44.
[2] Gomolka, R.S., et al. Elife, 2023. **12**.
[3] Lindhardt, T.B., et al. NMR Biomed, 2023: p. e5033.
[4] Giannetto MJ, et al. Glia. 2024.72(5): p.982-998.
[5] Constantinides, C. and K. Murphy. Front Cardiovasc Med, 2016. **3**: p. 23.
[6] Massey, C.A. and G.B. Richerson. J Neurophysiol, 2017. **118**(4): p. 2389-2401.
[7] Hablitz, L.M., et al. Sci Adv, 2019. **5**(2): p. eaav5447.
[8] Sullender, C.T., et al. J Neurosci Methods, 2022. **366**: p. 109434.

T13

Integrative Ecophysiology: MRI and MRS in View of Climate Change

Christian Bock[1]

[1]*Alfred Wegener Institute, Bremerhaven, Germany*

The ongoing and rapid climate change requires innovative methods and new fields of research to investigate and understand the impacts and changes in marine ecosystems. Climate-driven changes are already observable, particularly in the polar regions of the Arctic and Antarctic with their extreme environmental conditions, as these regions are considered the world's fastest-changing ecosystems. However, due to the extreme research conditions, the interactions within these sensitive and fragile ecosystems are still poorly understood.

A key organism in the Arctic Ocean is the polar cod (Boreogadus saida), which is considered a central link in the Arctic food web. Its connection to sea ice particularly underscores its importance in the context of ongoing climate change and shrinking ice masses. At the Alfred Wegener Institute, high-field MRI imaging and spectroscopy techniques are used either to observe the direct effects of changing environmental conditions on the physiology of marine organisms or to investigate long-term effects in longitudinal studies. A holistic experimental approach is employed, in which the organisms are continuously examined at all organizational levels—the whole animal, the circulatory system, organs, and cells—to obtain a comprehensive picture of physiological changes and their underlying mechanisms. This approach will be presented in detail using case studies on polar cod.

T14

Guardian of the Body‘s Inner Ocean: Probing the Tubule System with Quantitative MRI from Experimental Models to Humans

*Ehsan Tasbihi, **Thomas Gladytz**[1], Jose R. V. Vides, Jason M. Millward, Shahriar Shalikar, Erdmann Seeliger, Thoralf Niendorf*

[1]presenter: Max Delbrück Center for Molecular Medicine, Berlin, Germany

Introduction

Rising rates of kidney disease are a global concern, with inadequate biomarkers. The renal tubular volume fraction (TVF), the proportion of kidney tissue occupied by fluid-filled tubules, fluctuates with physiological conditions and is altered in disease, making it a promising non-invasive marker for assessing renal (patho)physiology and improving diagnostic precision. Magnetic resonance imaging (MRI) offers a forceful approach for the assessment of soft tissue architecture in the kidney. The transverse relaxation time T2 is a quantitative metric that reflects the loss of transverse magnetization caused by spin-spin interactions. We previously demonstrated the feasibility of this approach in rat kidneys by quantifying changes in TVF induced pharmacologically by furosemide administration as well as by a temporary increase in intratubular pressure1,2. The present translational study aims to quantify the tubular volume fraction for the first time in the human kidney using MRI in vivo and in a completely non-invasive manner. The primary objective of the present research endeavour is to establish a framework for conducting a non-invasive evaluation of micro-morphological alterations in renal tissue, in addition to assessing any concomitant functional changes in renal function, in patients.

Methods

Protocols were developed and optimized based on previously measured T2 relaxation times range in human kidney parenchyma and human urine measured in bladder and in vitro. Validation was performed with a phantom mimicking renal relaxation properties. All MR measurements were performed on a SkyraFit 3T system (Siemens Healthineers, Erlangen, Germany) using a 32-channel body RF coil (Siemens Healthineers) for signal reception and RF transmission. RARE module with (TR=3000ms, number of echoes=120, first TE=10ms, interecho time ΔTE=10ms, number of averages=1, tacquisition=6min58s) was employed to capture T2 information. For T2 mapping a mid-coronal oblique slice was acquired (in-plane spatial resolution=(960×960)μm2, FOV=(384×384)mm2, matrix size=400×400, slice thickness=5mm). Parallel imaging compressed

sensing (PICS) reconstruction was applied to estimate T2 maps directly from k-space data. TVF cartographies were calculated using voxel-wise bi-exponential fit of the T2 decay.

Results

Representative TVF maps were derived from NNLS analysis of T2 decays obtained from human kidney (Figure 1). TVF values were TVFCORTEX = 9.8% ± 1.5% (mean ± SEM, n = 2), TVFMEDULLA = 25.1% ± 1.2%.

Discussion

This work is the first in vivo visualization of tubular volume in kidney by using magnetic resonance. We demonstrate the feasibility of dynamic parametric mapping of the MRI relaxation time T2 for TVF cartography.

References

[1] Tasbihi, E., Gladytz, T., Millward, J. M., Cantow, K., Seeliger, E., & Niendorf, T. (2025). Magnetic Resonance Cartography of Renal Tubule Volume Fraction During Diuretic Intervention. Acta Physiologica, 241(9), e70095.

[2] Tasbihi, E., Gladytz, T., Millward, J. M., Periquito, J. S., Starke, L., Waiczies, S., ... & Niendorf, T. (2024). In vivo monitoring of renal tubule volume fraction using dynamic parametric MRI. Magnetic Resonance in Medicine, 91(6), 2532-2545.

T15

The Invisible Heat Revealed: Ultrafast MR Thermometry for Monitoring Thermal Therapy

Bruno Quesson[1]

[1]*University of Bordeaux, France*

This talk will present rapid MRI thermometry methods (using the PRFS approach) for monitoring tissue temperature changes under various experimental conditions. It will also cover the integration of real-time MR thermometry with MRI-compatible therapeutic devices (such as lasers, radiofrequency, and high-intensity focused ultrasound) to enable precise control of local heat deposition at targeted sites via a real-time feedback loop between temperature imaging and energy delivery. Applications of this method include irreversible thermal ablation, localized gene expression control, and targeted drug delivery. Finally, the advantages and limitations of high-field MRI thermometry will be discussed.

T16

Beyond: Metamaterial Antennas Enhance MRI of the Eye and Brain at 7.0 T

Nandita Saha, Bilguun Nurzed, Mostafa Berangi, Andre Kuehne, Helmar Waiczies, Igor Fabian Tellez Ceja, Xiang Hu, Thomas Gladytz, Lisa Krenz, Dave Huebler, Beate Endemann, Claudia Brockmann, Ebba Beller, Oliver Stachs, ***Thoralf Niendorf***[1]

[1] *presenter: Berlin Ultrahigh Field Facility (B.U.F.F.), Max Delbrück Center for Molecular Medicine in the Helmholtz Association and Charité – University Medicine, Berlin, Germany*

The problem: Unmet Needs

A growing number of reports document technical innovations in MRI of the eye and orbit and promote their application in translational research and clinical diagnostics. The delicate morphology of the eye and orbit requires imaging with sub-millimeter spatial resolution. Seizing this opportunity, new research directions and emerging clinical applications of ocular MRI are enabled by the sensitivity gains and spatial resolution enhancements afforded by UHF-MRI. Despite this progress, the potential of UHF-MRI of the eye and orbit is yet untapped, and the advantages are sometimes offset by a number of concomitant physics effects that bear the potential to spoil the benefits of UHF-MRI. The radiofrequency (RF) wavelength shortening at UHFs cause transmission field inhomogeneities, which may impair image quality. Dedicated RF coil arrays and parallel transmission techniques supporting transmit field modulation have been explored to enhance image quality in UHF-MRI of the eye and orbit. These approaches have been synergistically supported by high-permittivity dielectric pads. However, the pads remain constrained by geometry conditions, bulky design, and difficulty in integration with an anatomically adaptive RF coil.

Solution: Going Meta

Electromagnetic (EM) metamaterials (MTMs) present a viable alternative to dielectric pads. Prior MRI studies have explored flexible thin or bulk dielectric-based MTM surfaces as passive add-ons to conventional RF coils to improve receive sensitivity, but few have pursued true structural integration. Unlike add-on metamaterial surfaces, this presentation introduces metamaterial loaded antennas that can be directly implemented as a single integrated resonant structure to reshape transmit–receive fields via resonant or non-resonant near-field coupling. For proof-of-principle, we developed a multi-channel TX/RX metamaterial antenna (MTMA) for 7.0 T MRI. It was implemented in planar and bend configurations for neuro- and ocular imaging, with each design em-

bedding an MTM layer into a 2-channel loop array using a coplanar dual-layer approach.

Applications: MReye and beyond

Our phantom and in vivo studies demonstrate that the integrated metamaterial antenna enhance TX/RX performance through near-field coupling, effectively transforming a conventional loop array into a structurally unified MTM-enhanced antenna that functions as a single unified resonant system. The MTM antennae facilitated improvements in sensitivity, depth penetration and image uniformity for MRI of the eye, orbit, and occipital lobe of the brain.

Conclusion and Outlook

This presentation introduces clinically translatable metamaterial-integrated RF antenna (MTMA) customized for 7.0T MRI, establishing clinical application of electromagnetic metamaterials. It establishes metamaterials not as passive MRI enhancers, but as foundational components en-route to the development of next-generation, metamaterial-based, compact, anatomically tailored RF antennas for precision MRI.

T17

From Physics to Learning: Trustworthy AI as a Bridge in Quantitative MRI

Xinqi Li[1]

[1]*Max Delbrück Center for Molecular Medicine, Berlin, Germany*

Data-driven models have transformed medical image analysis, but many deep learning algorithms can struggle with generalization, interpretability, and physical plausibility, particularly in quantitative MRI. Xinqi would like to share ideas regarding how physics-informed AI combines mechanistic knowledge with the flexibility of data-driven methods, with practical experience in pharmacokinetic modeling, field correction, and test-time adaptation for quantitative cardiac MRI.

T18

MAGNETOM Terra.X: Progress in Clinical Ultrahigh Field MRI at 7.0 T

Jan Ruff[1]

[1]*Siemens Healthineers, Erlangen, Germany*

Ultra-high-field (≥7 tesla) magnetic resonance imaging has evolved from a research tool with approximately thirty installations in 2016 to an emerging clinical platform. Today more than one hundred systems are in operation, with approximately half being used in clinical settings. The vision is clear: every patient who can benefit from a 7T examination should have access to one.

This transition has been, and continues to be, driven by a structured roadmap of clinically approved hardware and software innovations.

- From single-transmit to parallel-transmit technology, overcoming the RF field inhomogeneities that historically limited diagnostic utility of 7T MRI.
- From parallel imaging to deep learning-based reconstruction, reducing acquisition times by approximately 50% while maintaining image quality.
- From anatomical imaging towards quantitative and metabolic assessment, with future releases expanding clinical applications into musculoskeletal imaging, magnetic resonance spectroscopy, and chemical exchange saturation transfer (CEST) imaging.

Discover new biomarkers – Translate them into clinical workflows – Apply them in patients.

Poster Abstracts

(In alphabetical order)

P1

Can Large Language Models Reason Through MRI Physics? A Simulation-Based Framework for Evaluating MRI Acquisition Parameter Interpretation

Dr. Muna AlMulla[1]

[1] *Department of Radiologic Sciences, College of Allied Health Sciences, Kuwait University, Kuwait*

Introduction

Large language models (LLMs) have demonstrated promising capabilities in radiology image interpretation and technical MRI knowledge assessment.[1-3] However, their ability to interpret image changes arising from controlled manipulation of MRI acquisition parameters remains poorly understood. We propose a simulation-based framework to investigate whether LLMs can reason through the MRI physics underlying image formation rather than simply recognising visual differences.

Methods

MRI image series were generated using a dedicated MRI simulation platform (Corsmed, Stockholm, Sweden), with systematic manipulation of individual acquisition parameters under controlled imaging conditions. Five large language models independently analysed the simulated image series using standardised prompts. Responses were independently reviewed using a structured MRI physics rubric, with the complete experimental workflow illustrated in Figure 2.

Results

Simulation enabled reproducible assessment of AI responses under controlled imaging conditions. LLMs generally recognised progressive image changes; however, considerable variation was observed in the consistency and completeness of MRI physics explanations. Differences were particularly evident when relating acquisition parameter manipulation to signal behaviour, tissue contrast and image-quality characteristics, illustrating that image recognition alone does not necessarily reflect accurate MRI physics reasoning.

Conclusion

MRI simulation offers a reproducible experimental framework for investigating AI understanding of MRI acquisition physics. Beyond evaluating image interpretation, simulation-based benchmarking provides an opportunity to characterise the strengths and limitations of AI reasoning in MRI and may contribute to the future development of educational and technical validation tools for MRI practice.

References

[1] Nakaura T, Kobayashi N, Masuda T, et al. Performance of State-of-the-Art Multimodal Large Language Models on an Image-Rich Radiology Board Examination: Comparison to Human Examinees. Academic Radiology. 2026;33(2):348–358.

[2] McMillan AB, et al. Performance of Large Language Models in Technical MRI Question Answering: A Comparative Study. arXiv. 2024.

[3] Radau PE. MRI-Eval: A Tiered Benchmark for Evaluating LLM Performance on MRI Physics and GE Scanner Operations Knowledge. arXiv. 2026.

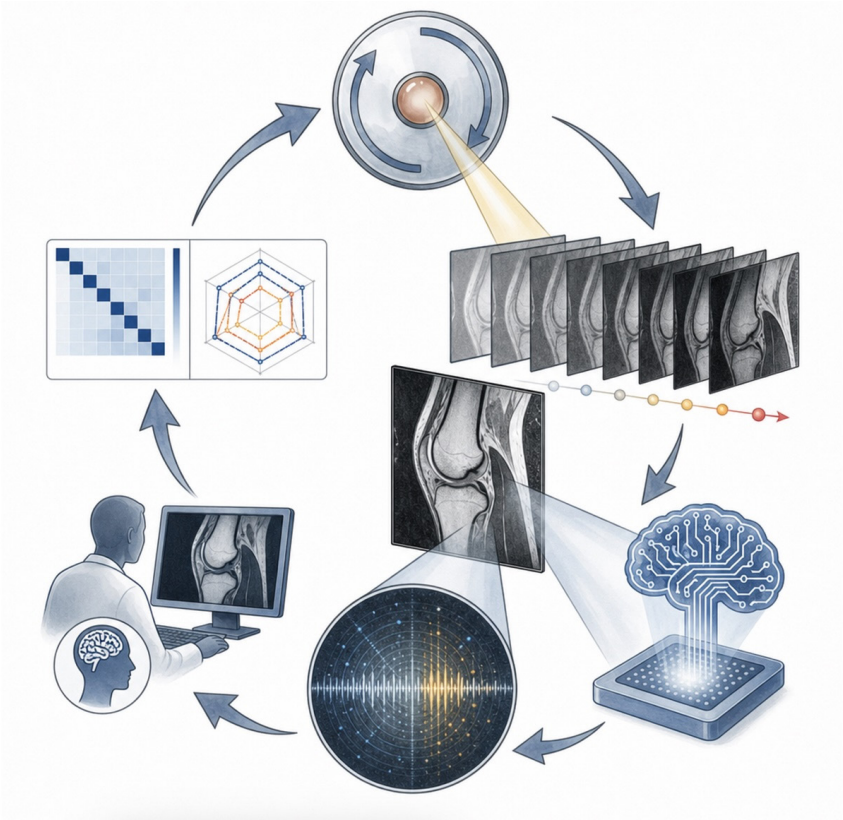

Figure 1

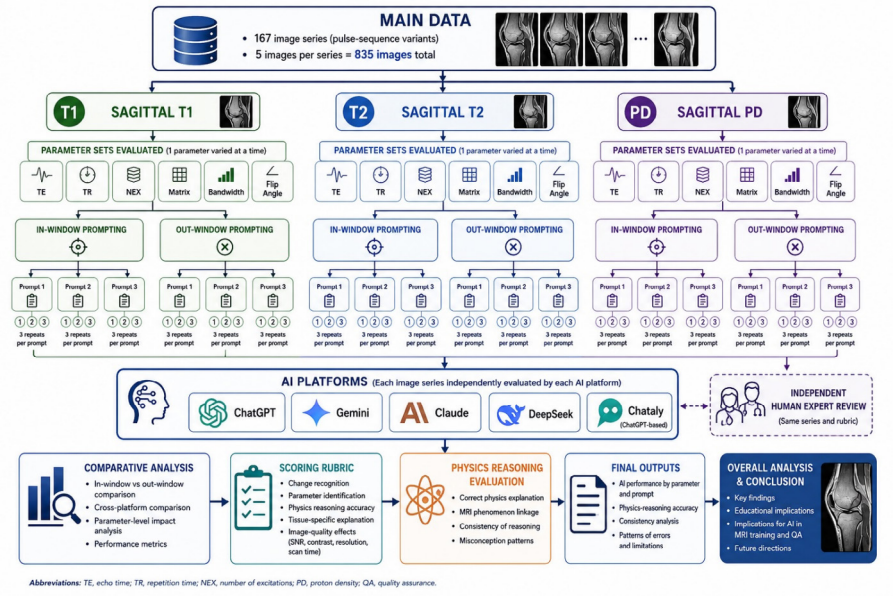

Figure 2

Picture description

Figure 1: Graphical abstract showing the simulation-based workflow for benchmarking LLM reasoning in MRI physics.

Figure 2: Overview of the simulation-based study workflow. A total of 167 MRI image series (835 images) were evaluated by five large language models across sagittal T1-, T2-, and PD-weighted sequences using multiple prompting strategies. AI responses were assessed using a standardised rubric to evaluate image recognition, MRI physics reasoning, and overall performance.

P2

Fluorine MR relaxation properties of fluorinated bioisosteres of evobrutinib

Lison Guillaume[1,2], Thomas Gladytz[1], Annaleah Hanske[3], Michael Dyrks[3], Marc Nazaré[3], Thoralf Niendorf[1,2,4], Sonia Waiczies[1,4]

[1]*Berlin Ultrahigh Field Facility (B.U.F.F.), Max Delbrück Center for Molecular Medicine in the Helmholtz Association, Berlin, Germany,*

[2] *Charité-Universitätsmedizin Berlin, Germany,*

[3]*Medicinal Chemistry Research Group, Leibniz-Forschungsinstitut für Molekulare Pharmakologie, Berlin, Germany,*

[4]*Experimental and Clinical Research Center (ECRC), A Joint Cooperation between the Charité Medical Faculty and the Max-Delbrück Center for Molecular Medicine in the Helmholtz Association, 13125 Berlin, Germany*

Introduction

Multiple sclerosis (MS) is an autoimmune disorder of the central nervous system. Bruton's tyrosine kinase inhibitors (BTKis) are promising during disease progression, as BTK is central in B cell and myeloid cell activation, drivers of chronic inflammation and neurodegeneration [1,2]. The BTKi evobrutinib has shown efficacy in MS clinical studies [3]. Fluorination could improve the theranostic properties and MR reporting of drugs, such as teriflunomide [4]. Here we investigated the MR relaxation properties of three fluorinated bioisosteres of evobrutinib: F-, trifluoromethyl (CF_3)- and pentafluorosulfanyl (SF_5)- evobrutinib.

Methods

The 3 bioisosteres were prepared at equal fluorine atomic concentration (2.5mM of F). MR measurements were performed at room temperature (RT) and at 37°C on a Bruker Biospec 9.4T pre-clinical MR scanner and $^{1}H/^{19}F$ mouse head coil. Longitudinal relaxation (T_1) was measured using Single Pulse method (TR= 100, 150, 200, 300, 400, 500, 750, 1000, 1500, 2000, 5000 ms). Transversal relaxation relaxation (T_2) was measured using Carr-Purcell-Meiboom-Gill (CPMG) method (Echo spacing= 2.188ms, Echoes= 256, TR= 2000 ms). All post-processing was performed with MATLAB R2019b.

Results and Discussion

Measurements revealed distinct T_1 and T_2 values among the three evobrutinib derivatives at RT and at 37°C (Figure 1). The F-labelled evobrutinib (Table 1) exhibited the longest T_2 at both temperatures, result of a slow transverse signal decay and therefore favourable properties for 19F MR detection; however, its T_1 was also the longest, which may limit acquisition efficiency due to slower signal recovery. For CF_3-labelled evobrutinib, both T_1 and T_2 increase from RT to 37°C,

demonstrating a temperature dependency of its relaxation behaviour. The SF_5-labelled evobrutinib showed the most favourable relaxation properties for rapid ^{19}F MR acquisition: the T_1 is shorter especially at 37°C indicating fast longitudinal signal recovery, corresponding to higher signal acquisition efficiency. While the T_2 is also the shortest, this remains well within a workable range, and is further supported by its large chemical shift separation, which enhances spectral discrimination. Pharmacodynamic assessment showed comparable BTK inhibitory activity (data not shown).

Conclusion

These findings identify the SF_5-bioisoster of evobrutinib as the most promising candidate for subsequent ^{19}F MR studies in blood–brain barrier organoids.

References

[1] Krämer J, Bar-Or A, Turner TJ, Wiendl H. Bruton tyrosine kinase inhibitors for multiple sclerosis. Nat Rev Neurol. 2023 May;19(5):289-304. doi: 10.1038/s41582-023-00800-7. Epub 2023 Apr 13.

[2] Pal Singh S, Dammeijer F, Hendriks RW. Role of Bruton's tyrosine kinase in B cells and malignancies. Mol Cancer. 2018 Feb 19;17(1):57. doi: 10.1186/s12943-018-0779-z. Erratum in: Mol Cancer. 2019 Apr 3;18(1):79. doi: 10.1186/s12943-019-1009-z.

[3] Montalban X, Vermersch P, Arnold DL, Bar-Or A, Cree BAC, Cross AH, Kubala Havrdova E, Kappos L, Stuve O, Wiendl H, Wolinsky JS, Dahlke F, Le Bolay C, Shen Loo L, Gopalakrishnan S, Hyvert Y, Javor A, Guehring H, Tenenbaum N, Tomic D; evolutionRMS investigators. Safety and efficacy of evobrutinib in relapsing multiple sclerosis (evolutionRMS1 and evolutionRMS2): two multicentre, randomised, double-blind, active-controlled, phase 3 trials. Lancet Neurol. 2024 Nov;23(11):1119-1132. doi: 10.1016/S1474-4422(24)00328-4. Epub 2024 Sep 19. Erratum in: Lancet Neurol. 2026 Apr;25(4):e10. doi: 10.1016/S1474-4422(26)00043-8.

[4] Prinz C, Starke L, Ramspoth TF, Kerkering J, Martos Riaño V, Paul J, Neuenschwander M, Oder A, Radetzki S, Adelhoefer S, Ramos Delgado P, Aravina M, Millward JM, Fillmer A, Paul F, Siffrin V, von Kries JP, Niendorf T, Nazaré M, Waiczies S. Pentafluorosulfanyl (SF5) as a superior 19F magnetic resonance reporter group: signal detection and biological activity of teriflunomide derivatives. ACS Sens. 2021 Nov 26;6(11):3948-3956. doi: 10.1021/acssensors.1c01717.

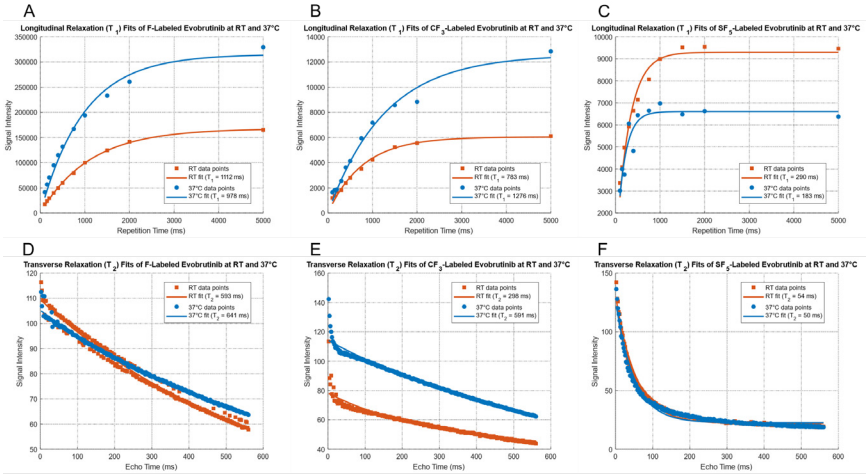

Figure 1

	F	CF_3	SF_5
T_1 at RT (ms)	1112	783	290
T_1 at 37°C (ms)	978	1276	183
T_2 at RT (ms)	593	298	54
T_2 at 37°C (ms)	641	591	50
Chemical shift (ppm)	-117.47	-58.80	65.98

Table 1

Picture description

Figure 1: Longitudinal (T_1) relaxation fits of F- (A), CF_3- (B) and SF_5- (C) labelled evobrutinib at RT and 37°C and Transverse (T_2) relaxation fits of F- (D), CF_3- (E) and SF_5- (F) labelled evobrutinib at RT and 37°C

Table 1: Relaxation parameters of F-, CF_3- and SF_5-labelled evobrutinib at RT and 37°C

P3

Metamaterial-integrated bow-tie antenna array for magnetic field shaping at 7T: a route towards RF phase-encoded B_1 and SAR steering

Jegyasu Gupta[1], Nandita Saha[1], Jose Raul Velasquez Vides[1], Shahriar Shalikar[1], Thoralf Niendorf[1,2]

[1]*Berlin Ultrahigh Field Facility (B.U.F.F.), Max Delbrück Center for Molecular Medicine in the Helmholtz Association, Berlin, Germany,*

[2] *Charité-Universitätsmedizin Berlin, Germany*

Introduction

At ultrahigh field MRIs, the RF wavelength in tissue approaches anatomical dimensions, causing transmit field inhomogeneity, reduced efficiency and elevated local SAR [1]. Electromagnetic metamaterials (MMs), periodic arrays of subwavelength resonant elements, permit tailored RF field shaping [2]. Most remain passive add-ons alongside a conventional coil; few pursue structural integration, where metamaterial and antenna form one near-field-coupled resonant system [3]. We design metamaterial-integrated bow-tie antenna (MM-BTA) arrays for transmit field enhancement, with a further focus on localization and SAR steering.

Methods

The unit cell (UC) combines a nested split-ring array with a bow-tie copper structure on 0.4 mm FR4. It is simulated in CST between two waveguide ports along z, with PEC on y and PMC on x, exciting the electric resonance at 297 MHz, matching the 7T Larmor frequency (−17.31 dB, −10 dB bandwidth 1.80 MHz, loaded Q ≈ 165). Each element is dual-layer and coplanar: a bow-tie antenna (BTA) with a central feed port and two lumped capacitors for tuning and matching, and a 4×4 periodic MM array on the reverse. Five MM-BTA elements are placed around the Duke voxel head model; an identical array without the MM layer serves as reference. Each element is fed from a single channel (P_1–P_5) with zero relative phase. Simulations at 297 MHz are normalised to 1W accepted power, with B_1^+ and SAR (10g) evaluated on co-registered orthogonal planes.

Results

The MM-BTA array produces a stronger, more homogeneous transmit B_1^+ distribution, most pronounced adjacent to the elements and extending inward. Over a central head ROI (±70 mm in-plane, sagittal view), the $|B_1^+|$ coefficient of variation fell from 61.8% (BTA) to 46.8% (MM-BTA). The SAR (10g) maps show

redistributed deposition, the reference scalp hotspot reduced with MM-BTAs. The transmit efficiency normalised to safety parameter, $B_1^+/\sqrt{(\text{peak spatial SAR (10g)})}$, was 0.1244 and 0.1771 $\mu T/\sqrt{(W/kg)}$ for the reference and MM-BTA arrays respectively, an increase of 42.4% [4].

Discussion and outlook

Structural integration modifies the near-field basis function of each element, rather than re-weighting fixed element fields, offering a complementary route to transmit field control at UHF. The axial B_1^+ asymmetry arises from unequal loading of the high-Q elements, absent in the broadband reference array. Per-element power redistribution and retuning are planned, followed by phase-encoded steering and phantom validation.

References

[1] M. E. Ladd et al., "Pros and cons of ultra-high-field MRI/MRS for human application," Prog Nucl Magn Reson Spectrosc, vol. 109, pp. 1-50, Dec 2018.

[2] A. Alipour, A. C. Seifert, B. N. Delman, P. R. Hof, Z. A. Fayad, and P. Balchandani, "Enhancing the brain MRI at ultra-high field systems using a meta-array structure," Med Phys, vol. 50, no. 12, pp. 7606-7618, Dec 2023.

[3] N. Saha et al., "Metamaterial Antennas Enhance MRI of the Eye and Occipital Brain," Advanced Materials, vol. 38, no. 32, p. e17760, 2026.

[4] P. S. Jacobs, W. Brink, A. Alipour, and R. Reddy, "A review of metamaterial and metasurface applications in magnetic resonance imaging," Magnetic Resonance Imaging, vol. 133, p. 110731, 2026.

[5] M. K. Woo et al., "A 16-Channel Dipole Antenna Array for Human Head Magnetic Resonance Imaging at 10.5 Tesla," Sensors, vol. 21, no. 21, 2021.

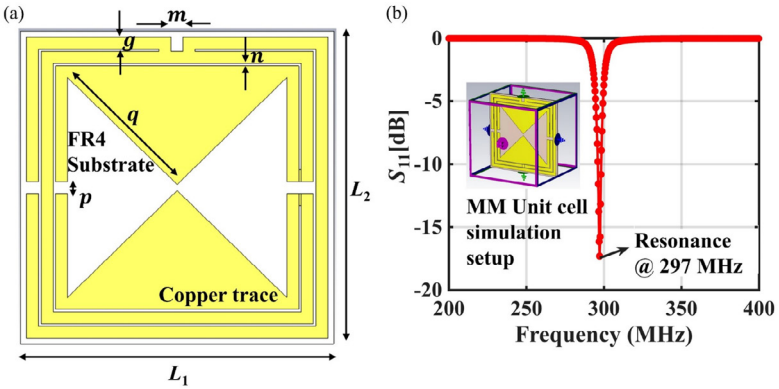

Figure 1

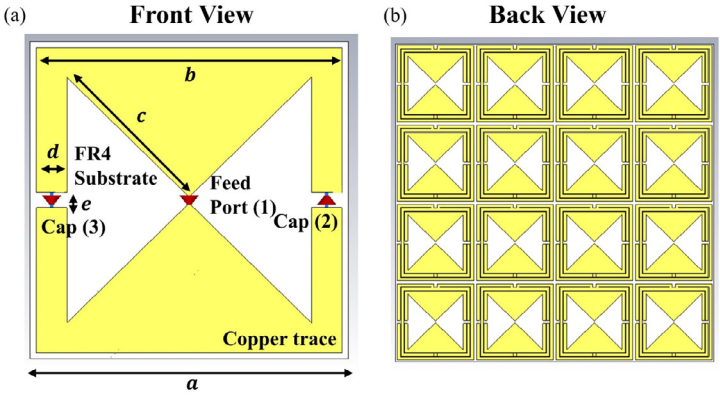

Figure 2

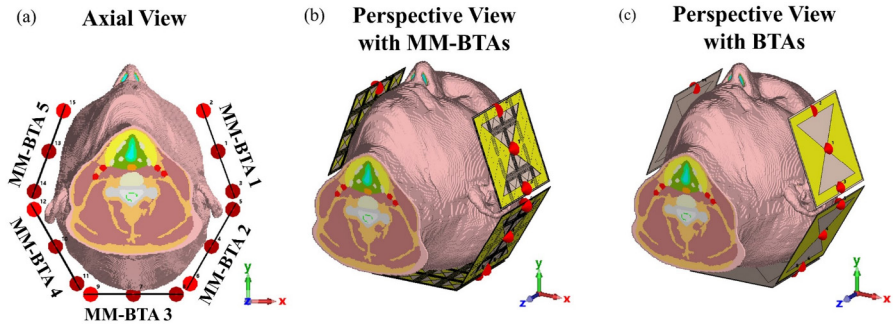

Figure 3

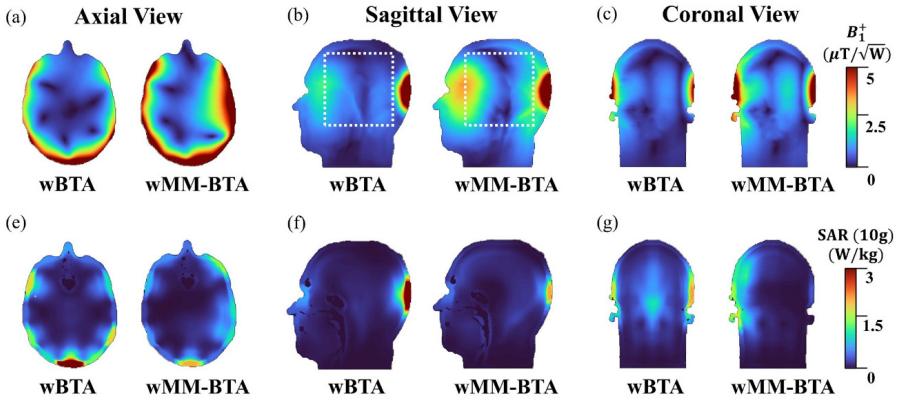

Figure 4

Picture description

Figure 1. (a) MM unit cell: nested split-ring array with bow-tie copper trace on FR4. The dimensions (in mm) of the UC are L1 = 26 mm, L2 = 25 mm, m = 1 mm, n = 0.2 mm, g = 1 mm, p = 1 mm, and q = 12.7 mm. (b) Reflection characteristics (S11[dB]) for UC.

Figure 2. MM-BTA transceiver element. (a) Front view: copper bow-tie, central feed port (marked as 1), two lumped capacitors (marked as 2 and 3). (b) Back view: 4 × 4 periodic MM layer on the same FR4 substrate.

Figure 3. Numerical analysis setup. (a) Axial view with five MM-BTA elements around the Duke voxel head model. (b) Perspective with MM-BTAs. (c) Reference array without the MM layer.

Figure 4. B1 and SAR (10g) distribution for the reference with BTA (wBTA) and metamaterial-integrated with MM-BTA (wMM-BTA) arrays for 1W accepted power. (a–c) B1+ distribution in axial, sagittal, and coronal planes. (e–g) Corresponding SAR (10g) distribution. The white dotted rectangle in Fig 4(b) shown considered ROI for the calculation of B1+ coefficient of variation.

P4

Uncovering Energetic Remodeling in Genetic Heart Disease by ^{31}P MRS

Yingke Hou[1,2,3], Karl-Heinz Herrmann[4], Marc Jonuscheit[5,6], Xinqi Li1,[7,8], Shalikar Shahriar[1,3], Verena Hoerr[9], Xiaomin Wang[1,2], Vera B. Schrauwen-Hinderling[5,6], Lucio Frydman[10,11], Thoralf Niendorf[1,3,12], Min-Chi Ku[1,2]

[1] *Berlin Ultrahigh Field Facility (B.U.F.F.), Max Delbrück Center for Molecular Medicine in the Helmholtz Association (MDC), Germany*

[2] *DZHK (German Centre for Cardiovascular Research), partner site Berlin, Berlin, Germany*

[3] *Charité-Universitätsmedizin Berlin, Berlin, Germany*

[4] *Institute of Diagnostic and Interventional Radiology, Medical Physics Group (MRI), University Hospital Jena, Jena, Germany*

[5] *Institute for Clinical Diabetology, German Diabetes Center (DDZ), Leibniz Center for Diabetes Research at Heinrich Heine University Düsseldorf, Düsseldorf, Germany*

[6] *German Center for Diabetes Research (DZD e.V.), München-Neuherberg, Germany*

[7] *Biomedical Imaging Research Institute, Cedars-Sinai Medical Center, United States*

[8] *TUM School of Computation, Information and Technology, Technische Universität München, Germany*

[9] *Department of Internal Medicine II, Cardiovascular Imaging Group, University Hospital Bonn, Bonn, Germany*

[10] *Department of Chemical and Biological Physics, Weizmann Institute of Science, Rehovot, Israel*

[11] *National High Magnetic Field Laboratory, Florida State University, Tallahassee, FL, United States*

[12] *Experimental and Clinical Research Center (ECRC), Max Delbrück Center for Molecular Medicine and Charité – Universitätsmedizin Berlin, Berlin, Germany*

Keywords: hypertrophic cardiomyopathy; ^{31}P-MRS; myocardial energetics; PCr/ATP; inorganic phosphate; creatine kinase flux; cryoprobe; mitochondria

Introduction

Energetic impairment is increasingly recognized as an early feature of hypertrophic cardiomyopathy (HCM). MYBPC3 mutations can reduce myocardial phosphocreatine (PCr)/ATP before the development of hypertrophy, fibrosis, or systolic dysfunction, suggesting that altered energetics may precede overt structural disease [1–7]. However, how energetic remodeling evolves in early disease progression and whether it reflects increased ATP demand, impaired mitochondrial supply, or disrupted energy transfer remains unknown.

^{31}P-MRS could provide mechanistic insight into these processes, but the low sensitivity of cardiac ^{31}P-MRS in mice represents a major barrier to longitudinal investigation.

Objective and Hypothesis: We established cryogenic-probe cardiac ^{31}P-MRS to overcome this sensitivity barrier and enable longitudinal characterization of

energetic remodeling in genetic-driven HCM. We hypothesized that enhanced sensitivity would reveal early energetic alterations and enable assessment of their progression and reversibility.

Methodology

Cardiac ^{31}P-MRS was performed on a Bruker BioSpec 94/20 9.4 T system in C57BL/6J Mybpc3 knock-in (KI) mice and wild-type (WT) littermates of both sexes. A dedicated ^{31}P cryoprobe was used to enhance cardiac ^{31}P-MRS sensitivity, together with a 72-mm quadrature ^{1}H room-temperature coil for anatomical localization (Figure 1A) [8]. Before ^{31}P-MRS, B0 mapping guided cardiac voxel shimming, followed by ^{31}P calibration. Cardiac- and respiratory-gated 3D-ISIS single-voxel ^{31}P-MR spectroscopy was acquired with TR = 4000 ms, 78 averages per ISIS step, 2048 complex data points, 7937 Hz spectral bandwidth, and an acquisition time of approximately 42 min[9] (Figure 1B). The voxel was positioned on end-diastolic localizers over the left-ventricular free wall; ECG and respiratory gating were applied throughout acquisition.

An initial baseline cohort of homozygous Mybpc3 KI mice and WT littermates (n = 6 per genotype) underwent cardiac ^{31}P-MRS, followed by spectral quality control, including assessment of peak resolution and separation, before metabolite quantification. The overall workflow included MRS setup, baseline assessment, matched intervention, repeat MRS, and endpoint tissue analyses, as summarized in Figure 1C.

Preliminary results

The representative ISIS voxel encompassed the entire LV, with well-resolved and undistorted ^{31}P spectra (Figure 2A). PCr/β-ATP was significantly reduced in KI compared with WT hearts (0.96 vs 2.47; −61%; p = 0.041), consistent across γ-ATP (0.72 vs 1.53; −53%; p = 0.009) and α-ATP (0.43 vs 1.24; −65%; p = 0.004) references (Figure 2B). Inter-ATP ratios remained unchanged (α-/β-ATP, p = 0.485; γ-/β-ATP, p = 0.937), making differential blood contamination or ATP-specific saturation unlikely because either would be expected to alter the relative ATP peak amplitudes [10]. Pi/PCr was markedly increased in KI (3.66 vs 0.37; p = 0.009), whereas Pi/β-ATP was not significantly altered (p = 0.132), supporting altered myocardial energetic homeostasis beyond isolated PCr depletion.

References

[1] Ommen SR, et al. 2024 AHA/ACC/multisociety guideline for the management of hypertrophic cardiomyopathy. Circulation. 2024.

[2] Carrier L, et al. Cardiac myosin-binding protein C (MYBPC3) in cardiac pathophysiology. Gene. 2015;573(2):188-197.

[3] Spudich JA. Three perspectives on the molecular basis of hypercontractility caused by hypertrophic cardiomyopathy mutations. Pflugers Arch. 2019;471(5):701-717.

[4] Toepfer CN, Wakimoto H, Garfinkel AC, et al. Myosin sequestration regulates sarcomere function, cardiomyocyte energetics, and metabolism, informing the pathogenesis of hypertrophic cardiomyopathy. Circulation. 2020;141(10):828-842.

[5] Crilley JG, et al. Hypertrophic cardiomyopathy due to sarcomeric gene mutations is characterized by impaired energy metabolism. J Am Coll Cardiol. 2003;41(10):1776-1782.

[6] Abraham MR, et al. Altered creatine kinase adenosine triphosphate kinetics in failing hypertrophied human myocardium. Circulation. 2006;114(11):1151-1158.

[7] Neubauer S. The failing heart, an engine out of fuel. N Engl J Med. 2007;356(11):1140-1151.

[8] Ratering D, et al. Performance of a 200-MHz cryogenic RF probe designed for MRI and MRS of the murine brain. Magn Reson Med. 2008;59(6):1440-1447.

[9] Bakermans AJ, et al. In vivo mouse myocardial 31P MRS using 3D ISIS: technical considerations and biochemical validations. NMR Biomed. 2015;28(10):1218-1227.

[10] Horn M, et al. 31P-NMR spectroscopy of blood: a species comparison. J Cardiovasc Magn Reson. 2000;2(2):143-151.

[11] Kalsi KK, Smolenski RT, Pritchard RD, Khaghani A, Seymour A-ML, Yacoub MH. Energetics and function of the failing human heart with dilated or hypertrophic cardiomyopathy. Eur J Clin Invest. 1999;29(6):469-477.

[12] de Wit-Verheggen VHW, Schrauwen-Hinderling VB, Brouwers K, et al. PCr/ATP ratios and mitochondrial function in the heart. A comparative study in humans. Sci Rep. 2023;13:8346.

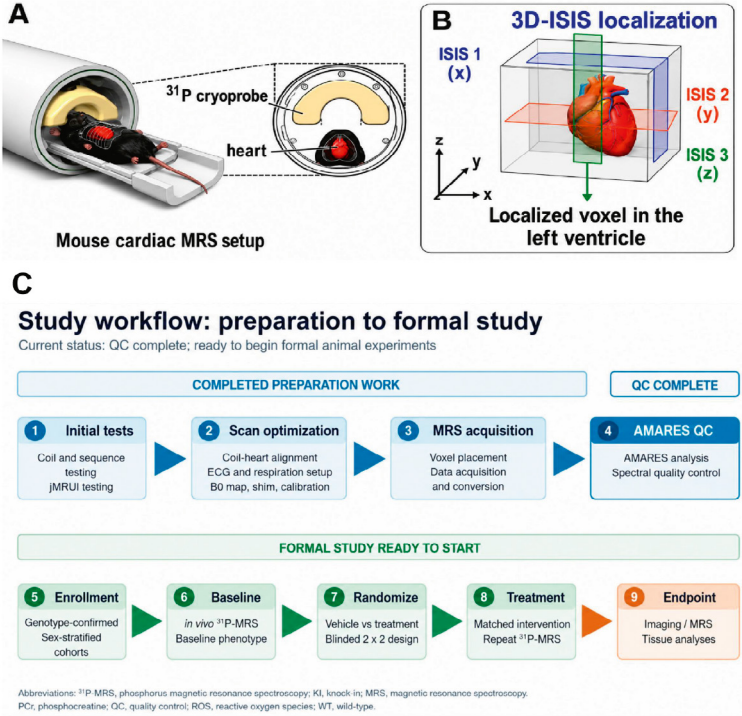

Figure 1

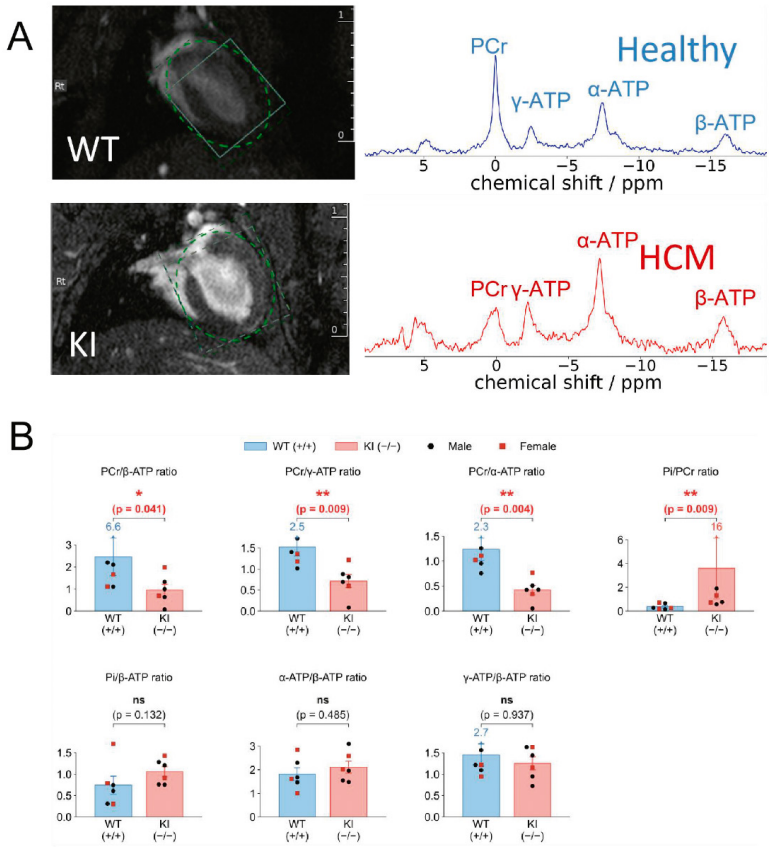

Figure 2

Figure description

Figure 1. Cardiac ^{31}P-MRS setup, localization, and study workflow.
(A) Mouse cardiac MRS setup using a dedicated ^{31}P cryoprobe and anatomical localization coil. (B) 3D-ISIS localization of the cardiac voxel in the left ventricle. (C) Study workflow from preparation and quality control to enrollment, baseline ^{31}P-MRS, randomization, intervention, repeat MRS, and endpoint imaging/tissue analyses."

Figure 2. Mybpc3-KI mice show reduced myocardial PCr/ATP and increased Pi/PCr ratios by ^{31}P-MRS. (A) Representative cardiac MR images and ^{31}P-MRS spectra from WT (+/+) and KI (−/−) mice. (B) PCr/ATP ratios were reduced and Pi/PCr ratio was increased in KI mice compared with WT mice, while ATP reference ratios were unchanged. Data are mean ± SEM; n = 6 per genotype;
Mann–Whitney U test; *p < 0.05, **p < 0.01."

P5

Evaluation of Image Contrast-Agnostic Brain MRI Segmentation on Heterogeneous Clinical Data

Elias Pilgrim[1], Kevin Rostásy[2], Friedemann Paul[3], Judith Bellmann-Strobl[3,4], Thoralf Niendorf[1,3], Sonia Waiczies[1,3], ***Jason Michael Millward[1,3] (presenter)***

[1]*Berlin Ultrahigh Field Facility (B.U.F.F.), Max Delbrück Center for Molecular Medicine in the Helmholtz Association, Berlin, Germany,*

[2]*Department of Paediatric Neurology, Children's Hospital Datteln, Witten/Herdecke University, Datteln, Germany.*

[3]*Experimental and Clinical Research Center (ECRC), a Joint Cooperation Between the Charité Medical Faculty and the Max-Delbrück-Center for Molecular Medicine in the Helmholtz Association, Berlin, Germany,*

[4]*NeuroCure Clinical Research Center, Charité-Universitätsmedizin Berlin, Freie Universität Berlin, Humboldt Universität zu Berlin, Berlin Institute of Health, Berlin, Germany*

Retrospective analysis of clinical magnetic resonance imaging (MRI) data is often challenging with heterogeneous and incomplete datasets. SynthSeg is a brain segmentation tool reportedly agnostic to MRI contrast and spatial resolution. We evaluated SynthSeg in a heterogeneous multi-center cohort of pediatric patients with acute disseminated encephalomyelitis, adults with multiple sclerosis (MS), and healthy pediatric subjects. Using matched pairs from the same subjects on the same day, we compared brain volumes between T1- vs. T2-weighted scans, before vs. after gadolinium-based contrast agent administration, and high vs. low-resolution scans. SynthSeg-derived volumes showed high correlation across matched scan pairs, with better performance for larger brain structures. Significant differences were detected between T1- and T2-weighted, and pre- vs. post-contrast scans, although effect sizes were modest. Low resolution images underestimated volumes, especially for smaller structures. Contrast-enhancing MS lesion volume or count had no significant effect on volumes of brain structures. T2 lesion volume or count showed no significant main effect, but a significant interaction, suggesting T2 lesions could affect analyses combining volumes from T1- and T2-weighted images. These results support SynthSeg for analysis of heterogeneous and incomplete MRI data, including combining volumes from images with different contrast or resolution, provided appropriate statistical methods are used.

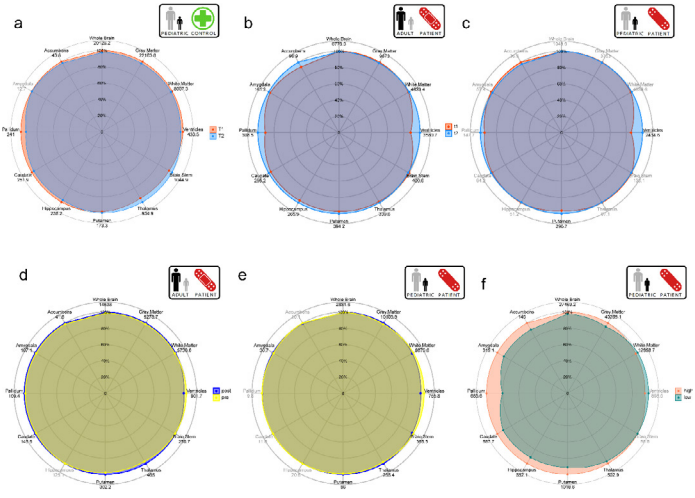

Figure 1

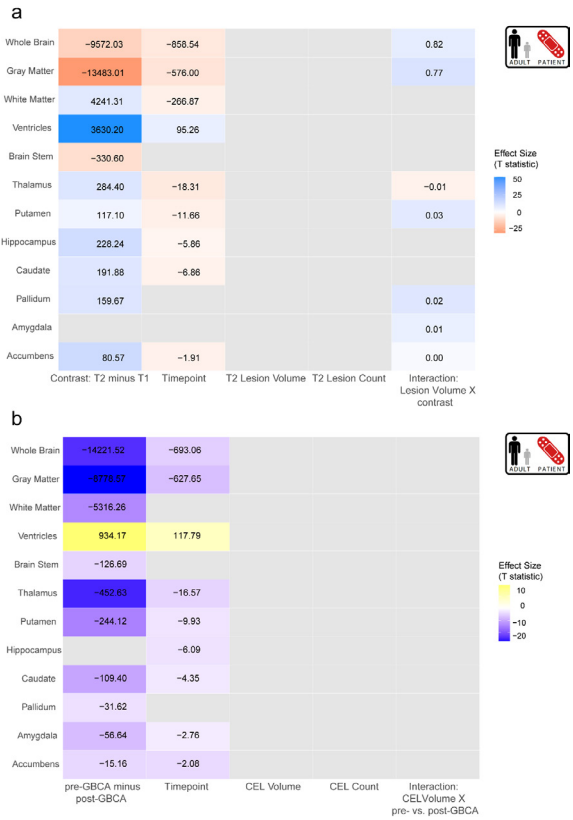

Figure 2

Picture description

Figure 1: Comparison of SynthSeg-derived brain volumes from matched MRI scans in patients and controls. (a) Spider plot shows absolute volume differences (mm^3) of 12 brain structures derived from matched T1- (red) and T2-weighted (blue) images acquired from healthy pediatric subjects during the same MRI scan session (n=630). Structures are arranged clockwise in descending order of size. Structures in black showed statistically significant differences between T1- and T2-weighted images (Wilcoxon signed rank test). Structures in grey showed no significant differences. Comparison of matched T1- and T2-weighted scans from (b) adult MS patients (n=37) and (c) pediatric ADEM patients (n=30). Comparison of matched scans before (yellow) and after (blue) administration of gadolinium contrast agent in (d) adult MS patients (n=35) and (e) pediatric ADEM patients. (f) Comparison of matched high resolution (1mm isotropic, red) and low resolution (blue) scans in pediatric ADEM patients in the same scan session (n=17).

Figure 2. Influence of T2-enhanced and gadolinium-enhancing lesions on SynthSeg-derived brain volumes in adult RRMS patients. Heatmaps show the results of linear mixed-effects models (LME) for twelve brain structures (arranged in descending order of size); colour indicates the effect size (t-statistic). Parameters with no significant effect on a structure are shown in grey. The values of the beta coefficients (absolute effect of the parameter in mm3) for significant effects are shown in the cells. Positive values indicate a given parameter increases the volume of a structure; negative values indicate a parameter decreases the volume of a structure. (A) Effects of T2-enhanced lesions on SynthSeg-derived structures. The LME includes the differences between T1- and T2-weighted images, the effect of time, T2 lesion volume, T2 lesion count, and the interaction between lesion volume and the T1- vs. T2 differences. T2 lesion volume and count did not have a significant effect on the volume of any structure. Lesion volume had a significant interaction for 7/12 structures, indicating that for these structures, T2 lesion volume significantly influenced the differences between T1 and T2-weighted volumes. (B) Effects of gadolinium-enhancing lesions of SynthSeg-derived structures. The LME includes the differences pre- and post-administration of gadolinium-based contrast agent (GBCA), the effect of time, contrast-enhancing lesion (CEL) volume, CEL count, and the interaction between CEL volume and the pre- vs. post-GBCA differences. CEL volume or count did not have a significant effect on the volume of any structure. The CEL volume did not have any significant interaction with the pre- vs. post-GBCA differences.

P6

Silicon Integrated RF Electronics for Low-Noise Multichannel UHF MRI

Christof Pfannenmüller[1], Fabian Schneider[1], Zeyi Chen[1], Fabian Lurz[1]

[1]Otto-von-Guericke University, Magdeburg, Germany

Noise figure of low-noise amplifiers (LNAs) is a key metric to increase signal-to-noise ratio (SNR) in modern MRI systems. With increasing amounts of channel therefore cost and hardware effort significantly increases [1].

Consequently silicon integration of dedicated RF front-ends provides a reasonable solution to provide high performance receive chains with low noise figure [2].

Within the project “Universal Integrated Console for Ultra-High-Field Magnetic Resonance Imaging” (UIC4UHFMRI) a heterogeneous integrated RF console for 14T MRI applications is developed.

According to Moore’s law the use of dedicated silicon integrated circuits (ICs) provides the ability to increase the number of channels within an RF system at nearly constant costs. Namely the setup cost for a silicon integrated device, e.g. an amplifier, mainly define the device costs, rather than the number of fabricated samples.

Corresponding silicon designs were created and circuit-level as well as electromagnetic simulations are used to evaluate gain, noise figure, input impedance, S-parameters, and linearity across the target frequency range. The IHP 130 nm silicon–germanium BiCMOS technology was utilized, as the high ohmic substrate is expected to provide minimum parasitic effects caused by magnetic field. Effects of bond wires and required single external matching components are taken into account.

Currently two system blocks have already been brought to fabrication by the foundry:

a LNA with a noise figure of 0.36 dB and a gain of 28.5 dB within a frequency range of 566 MHz to 697 MHz. The device is optimized for an input impedance of approximately Zin = 3 Ω. Therefore decoupling of mutual coils can be increased to improve SNR [3].

Further a voltage controlled oscillator (VCO) with a tuning range of 3.34 GHz to 5.71 GHz and a FoMt = -189,18 dBc/Hz was finished, intended to use with a frequency divider and mixer stage to convert the signals from Lamor frequency to baseband for digitization.

Utilizing a frequency divider therefore the evaluation of 1H, 2H, 13C, 19F, 23Na, 31P, and 39K could be shown in simulation for either 1.5T, 3T 7T and 14T field strengths.

Therefore, the building blocks allow for a universal console that could be used with various applications up to Ultra-High-Field and will be used within the console design.

Components like power amplifiers and AD-converters are subject to further research and development within the UIC4UHFMRI project.

With the fabricated silicon evaluation of high magnetic field influences are currently prepared and will be deducted in future.

References

[1] R. Pohmann, O. Speck, and K. Scheffler, “Signal-to-noise ratio and MR tissue parameters in human brain imaging at 3, 7, and 9.4 tesla using current receive coil arrays,” Magnetic Resonance in Medicine, vol. 75, no. 2, pp. 801–809, 2016.

[2] A. Rouhafza, R. L. Lagore, G. Adriany, K. Ugurbil, and Y. Tousi, “A 0.3dB-NF SiGe LNA Array for 10.5T Multi-Channel MRI Receivers,” in 2025 IEEE/MTT-S International Microwave Symposium - IMS 2025, 2025, pp. 202–205.

[3] F. Schneider, C. Pfannenmüller, A. Jöstingmeier, M. Ehses, G. Simone, B. Smith, H. Maune, and F. Lurz, “Measurement uncertainties of highly reflective low-noise-amplifiers for magnetic resonance imaging,” in 2026 107th ARFTG Microwave Measurement Conference (ARFTG), 2026, pp. 1–4.

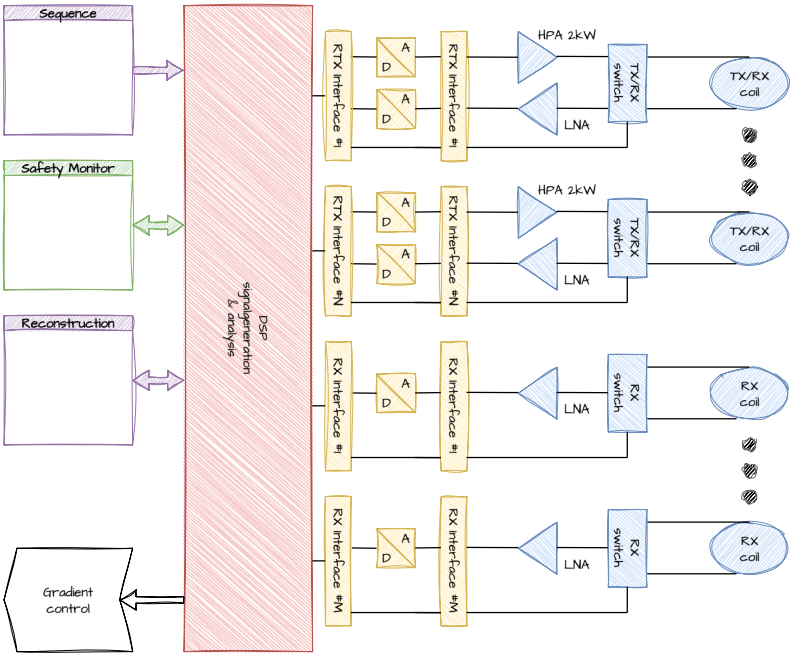

Figure 1

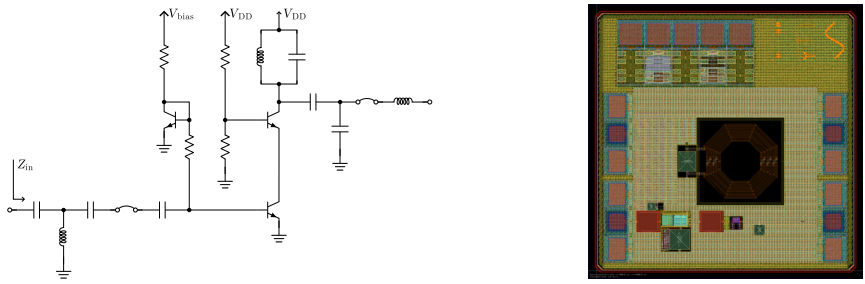

Figure 2

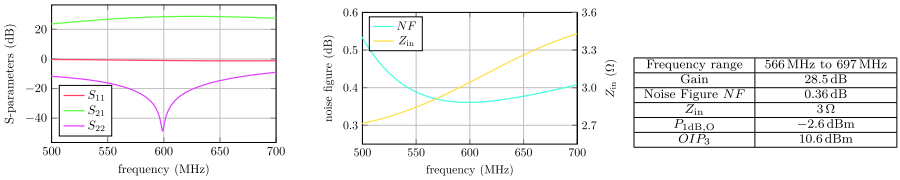

Frequency range	566 MHz to 697 MHz
Gain	28.5 dB
Noise Figure NF	0.36 dB
Z_{in}	3 Ω
$P_{1dB,O}$	−2.6 dBm
OIP_3	10.6 dBm

(c)

Figure 3

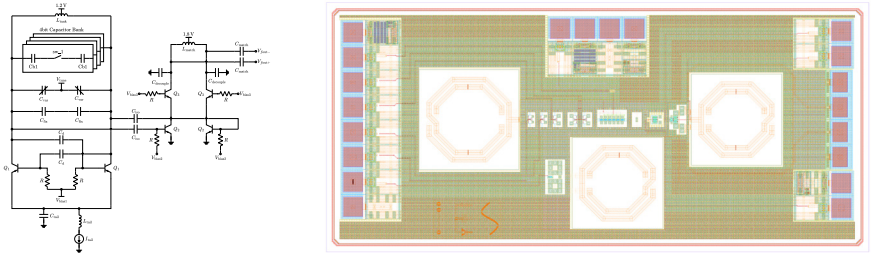

Figure 4

Picture description

Fig. 1: UIC4UHFMRI project overview and building blocks.

Fig. 2: LNA schematic and silicon IC layout utilizing a silicon area of 1 mm x 1 mm.

Fig. 3: Simulated S-Parameters, NF and Input Impedance of the proposed LNA and performance table of fabricated silicon LNA.

Fig. 4: VCO schematic and silicon IC layout utilizing a silicon area of 2.19 mm x 1 mm.

P7

Cardiac Phase–Resolved T_1 and T_2* relaxometry in Murine Hearts

Shahriar Shalikar[1,2], Xiaomin Wang[1,2], Jose Raul Velasquez Vides[1,4], Thomas Gladytz[1], Mostafa Berangi[1], Jason M. Millward[1,5], Thoralf Niendorf[1,3,5], Frank Kober[6], Min-Chi Ku[1,3]

[1] *Max-Delbrück-Center for Molecular Medicine in the Helmholtz Association (MDC), Berlin Ultrahigh Field Facility (B.U.F.F.), 13125 Berlin, Germany*

[2] *Charité-Universitätsmedizin, corporate member of Freie Universität Berlin and Humboldt-Universität zu Berlin,10117 Berlin, Germany*

[3] *DZHK (German Centre for Cardiovascular Research), partner site Berlin, Germany.*

[4] *Institute for Medical Engineering, Otto von Guericke University, Magdeburg, Germany.*

[5] *Experimental and Clinical Research Center (ECRC), a joint cooperation between the Charité Medical Faculty and the Max-Delbrück Center for Molecular Medicine, Berlin, Germany.*

[6] *Aix-Marseille Univ, CNRS, CRMBM, Centre de Résonance Magnétique Biologique et Médicale, Marseille, France.*

Introduction

Comprehensive myocardial tissue characterization is essential for understanding cardiovascular disease mechanisms, particularly in preclinical animal models that permit detailed investigation of disease progression and treatment effects. T_1 and T_2* mapping provide complementary information about myocardial composition and microstructure. T_1 reflects changes in water content, extracellular volume, and fibrosis, whereas T_2* is sensitive to magnetic susceptibility effects related to oxygenation, iron content, microvascular integrity, and tissue architecture. Combined assessment of T_1 and T_2* may therefore improve sensitivity to early pathological alterations such as fibrosis, edema, ischemia, and altered oxygen metabolism [1-4]. However, simultaneous mapping in rodents remains technically challenging due to rapid cardiac motion, small anatomy, and physiological motion artifacts. Here, we propose a retrospective cardiac phase–resolved reconstruction approach enabling simultaneous T_1 and T_2* mapping and evaluates its feasibility in a pilot mouse study.

Methods

A global inversion-recovery (IR) preparation was combined with a multi-gradient-echo (MGE) acquisition to encode joint T_1 and T_2* contrast in a single continuous scan (shown in Figure 1). This was evaluated *in vivo* at 9.4 T in a healthy 27-week-old male wild-type C57BL/6J mouse. A total of 228 inversion pulses were applied. Each IR block contained 300 MGE segments (TR = 15 ms; TE/ΔTE = 2.5/2.1 ms; FA = 10°; matrix = 128 × 128; slice thickness = 1 mm; GRAPPA factor = 1.68), followed by 1000 ms recovery. Data were acquired continuous-

ly using sequential phase encoding and retrospectively reconstructed into 10 cardiac phases, 5 echo times, and 10 inversion times. Pixel-wise fitting across inversion times and echo times generated cardiac phase-resolved T_1 and T_2* maps. Accuracy was assessed in a multi-vial phantom spanning the physiological myocardial T_1 and T_2* range, using conventional MGE-based T_2* mapping and Look-Locker T_1 mapping as reference methods.

Results

Phantom measurements from the proposed method agreed with conventional MGE T_2* and Look-Locker T_1 reference measurements ($R2 \approx 1$, $R2 \approx 1$) (Figure 2). Retrospectively reconstructed mid-ventricular short-axis images showed clear myocardial anatomy and no noticeable ghosting artifacts (Figure 3). Our method enabled efficient sampling of IR, multi-echo, and cardiac phase dimensions within one acquisition. Figure 3A shows CINE anatomical images; Figures 3B and 3C show IR images and multi-echo images with corresponding maps. CINE T_1 and T_2* maps are shown in Figures 4B and 4C. In the healthy mouse left ventricular myocardium, mean T_1 and T_2* values were 968 ± 321 ms and 6.7 ± 2.9 ms, respectively. Phase-resolved maps demonstrated temporal variation in both parameters over the cardiac cycle.

Discussion

Our results demonstrate the feasibility of CINE simultaneous T_1-T_2* mapping in the healthy murine myocardium, enabling multiparametric tissue characterization. The measured native myocardial T_1 values are in agreement with previously reported findings [5]. The T_2* values fall within expected physiological ranges [6], indicating no evidence of iron deposition or hemorrhagic alterations. Our approach mitigates motion-related artifacts, eliminates slice misregistration associated with sequential mapping techniques, and yields high-resolution parametric maps across the cardiac cycle. Simultaneous estimation of both parameters within a single acquisition reduces variability arising from physiological changes.

Conclusion

Simultaneous CINE T_1 and T_2* mapping provides a foundation for integrated and comprehensive assessment of myocardial tissue properties. Our multidimensional relaxometry may provide the sensitivity to detect early myocardial changes, to enhance the study of cardiovascular disease mechanisms and treatment effects. While the current implementation assumes motion-robust conditions and was validated in healthy mice, the work will be extended to study animal models of cardiometabolic disease. Future work will include further op-

timization of motion compensation and sequence robustness, harmonizing the protocol with human 3T scanners, to enable validation of T_1–T_2*-based CMR biomarkers and clinical translation.

References

[1] T. Cao et al., Free-breathing, non-ECG, simultaneous myocardial T1, T2, T2*, and fat-fraction mapping with motion-resolved cardiovascular MR multitasking," *Magnetic Resonance in Medicine*, vol. 88, no. 4, pp. 1748-1763, 2022.

[2] M. Heilmann et al., "Simultaneous dynamic T 1 and T 2* measurement for AIF assessment combined with DCE MRI in a mouse tumor model," *Magnetic Resonance Materials in Physics, Biology and Medicine*, vol. 20, no. 4, pp. 193-203, 2007.

[3] G. J. Lima da Cruz, C. Velasco, B. Lavin, O. Jaubert, R. M. Botnar, and C. Prieto, "Myocardial T1, T2, T2*, and fat fraction quantification via low-rank motion-corrected cardiac MR fingerprinting," *Magnetic Resonance in Medicine*, vol. 87, no. 6, pp. 2757-2774, 2022.

[4] I. Hermann, P. Kellman, O. B. Demirel, M. Akçakaya, L. R. Schad, and S. Weingärtner, "Free-breathing simultaneous T1, T2, and T2∗ quantification in the myocardium," *Magnetic resonance in medicine*, vol. 86, no. 3, pp. 1226-1240, 2021.

[5] S. Bohl et al., "Advanced methods for quantification of infarct size in mice using three-dimensional high-field late gadolinium enhancement MRI," *American Journal of Physiology-Heart and Circulatory Physiology*, vol. 296, no. 4, pp. H1200-H1208, 2009.

[6] O. Laghzali et al., "Cardiac Phase-Resolved T2* Magnetic Resonance Imaging Reveals Differences Between Normal Hearts and a Humanized Mouse Model of Hypertrophic Cardiomyopathy," *Biomedicines*, vol. 13, no. 5, p. 1193, 2025.

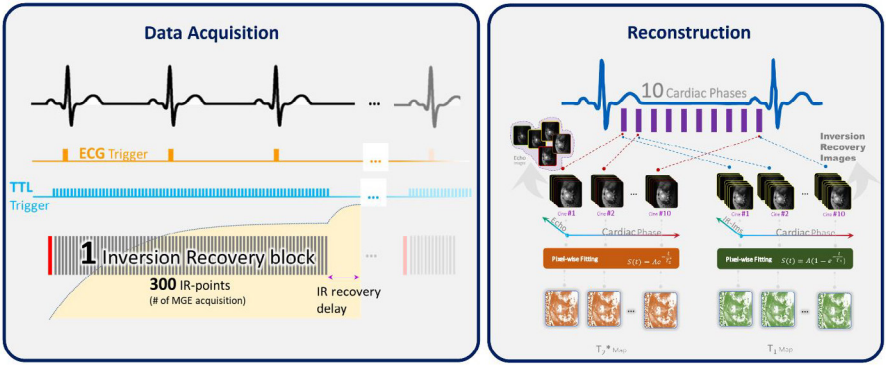

Figure 1

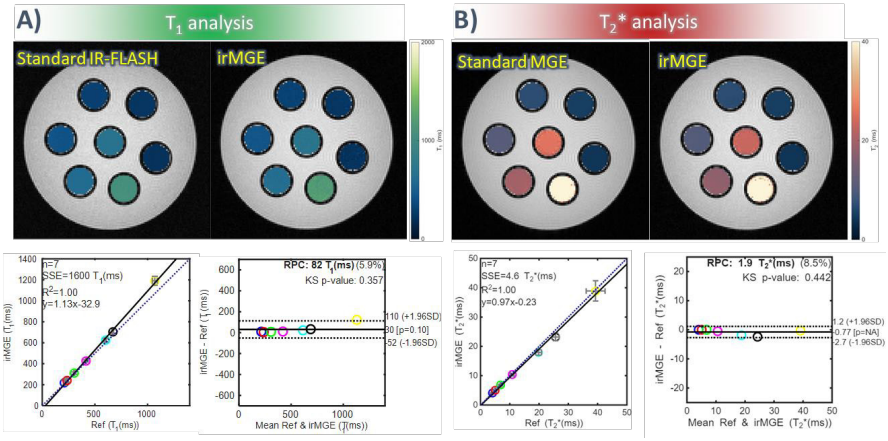

Figure 2

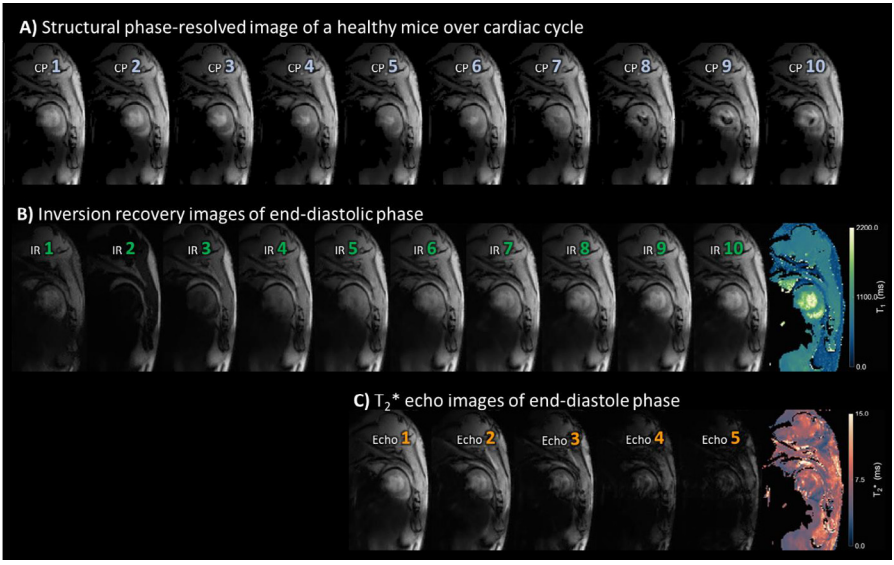

Figure 3

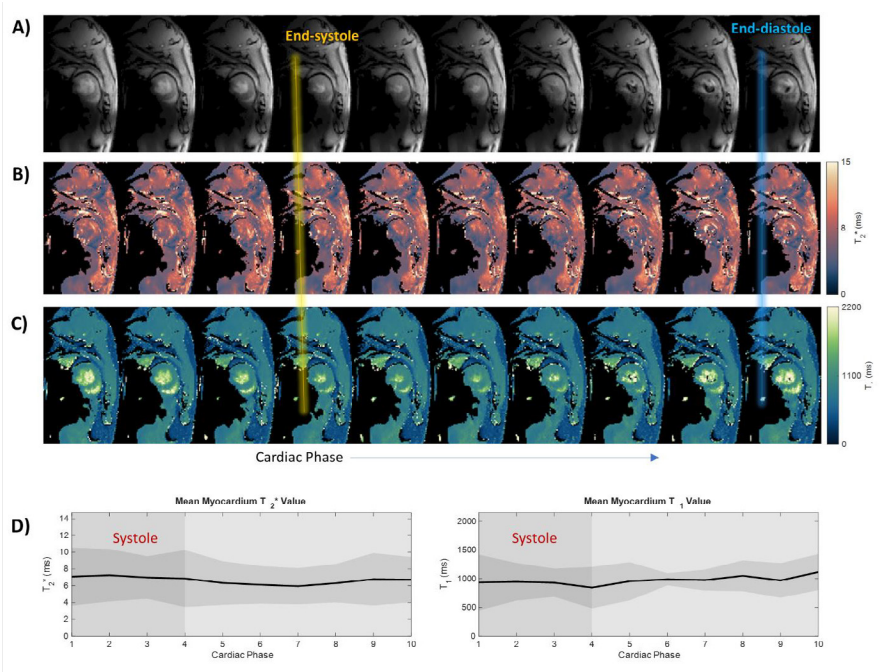

Figure 4

Picture description

Figure 1. Workflow of the developed framework for simultaneous cine T_1 and T_2* mapping. Imaging was carried out with a 2D multi-gradient echo sequence incorporating inversion recovery preparation. The collected data were retrospectively organized based on cardiac phase, inversion time, and echo time, followed by image reconstruction and voxel-wise model fitting to derive T_1 and T_2* parameter maps.

Figure 2. Phantom validation of simultaneous T_1 and T_2* mapping. Phantom contains 7 vials with known T1 and T2* spanning the physiological myocardial range. T_1 (A) and T_2* (B) values derived from the proposed method compared separately with standard sequence using linear regression and Bland–Altman analyses, demonstrating agreement between methods. irMGE: Inversion Recovery Multi-Gradient-Echo."

Figure 3. Representative raw images of a healthy mouse heart in a mid-ventricular SAX-view acquired on a 9.4T small-animal scanner, and reconstructed using the proposed cine simultaneous T_1 and T_2* mapping approach. (A) Cine anatomical images. (B) Echo images reconstructed at the end-diastolic phase corresponding to the last inversion recovery time point. (C) Inversion recovery images acquired at the same cardiac phase and the first echo time. SAX: Short-Axis-view; CP: cardiac Phase; IR: Inversion Recovery.

Figure 4. Cine simultaneous T_1 and T_2* mapping of a healthy mouse heart at the mid-SAX slice was performed on a 9.4T scanner using retrospective gating technique. (A) Structural images, (B) T_1 maps, and (C) T_2* maps are shown across the cardiac cycle. (D) Dynamic analysis of mean myocardial T_1 and T_2* values demonstrate temporal variation throughout the cardiac cycle."

P8

Multiparametric CMR Reveals Early Myocardial Perfusion Deficits Alongside Alterations in Diastolic Function in Hypertrophic Cardiomyopathy

Xiaomin Wang[1,2,3], Yingke Hou[1,2,3], Shalikar Shahriar[1,3], Frank Kober[4], Lucie Carrier[5,6], Thoralf Niendorf[1,3,7], Min-Chi Ku[1,2]

[1] *Berlin Ultrahigh Field Facility (B.U.F.F.), Max Delbrück Center for Molecular Medicine in the Helmholtz Association (MDC), Berlin, Germany*

[2] *DZHK (German Centre for Cardiovascular Research), partner site Berlin, Berlin, Germany*

[3] *Charité - Universitätsmedizin Berlin, Berlin, Germany*

[4] *Aix-Marseille Univ, CNRS, CRMBM, Centre de Résonance Magnétique Biologique et Médicale, Marseille, France.*

[5] *Department of Experimental Pharmacology and Toxicology, University Medical Center Hamburg-Eppendorf, 20246 Hamburg, Germany; l.carrier@uke.de.*

[6] *DZHK (German Centre for Cardiovascular Research), partner site Hamburg/Kiel/Lübeck, 20246 Hamburg, Germany.*

[7] *Experimental and Clinical Research Center (ECRC), Max Delbrück Center for Molecular Medicine and Charité - Universitätsmedizin Berlin, Berlin, Germany*

Keywords: cardiomyopathy; myocardial strain; myocardial perfusion; diastolic function; time-volume curve; quantitative CMR

Introduction

*MYBPC*3 haploinsufficiency is a leading genetic cause of hypertrophic cardiomyopathy (HCM), but heterozygous carriers may remain clinically silent despite subclinical myocardial abnormalities [1,2]. This heterozygous *Mybpc*3 point-mutation model enables study of subclinical HCM, where changes in myocardial deformation, microvascular function, and filling may precede overt systolic dysfunction. Diet-induced obesity and/or vascular stress may unmask latent phenotypes [3,4]. We tested whether multiparametric cardiovascular magnetic resonance (CMR) detects *Mybpc*3- and stress-related changes beyond conventional cine function.

Methodology

Wild-type (WT), heterozygous *Mybpc*3 targeted knock-in (HET), and homozygous knock-in mice received chow or high-fat diet (HFD). HFD plus N^{ω}-nitro-L-arginine methyl ester (L-NAME) assessed additional metabolic and vascular stress [4]. After 4–5 months of intervention, CMR was performed at 9.4 T with cardiac and respiratory gating. Cine CMR quantified ventricular function, wall thickness, left ventricular (LV) mass/end-diastolic volume (EDV), strain, and time–volume filling/ejection indices. Arterial spin labeling(ASL) measured re-

gional diastolic and systolic myocardial blood flow (MBF); ΔMBF was defined as diastolic minus systolic MBF [5,6]. Models adjusted for sex and heart rate where feasible.

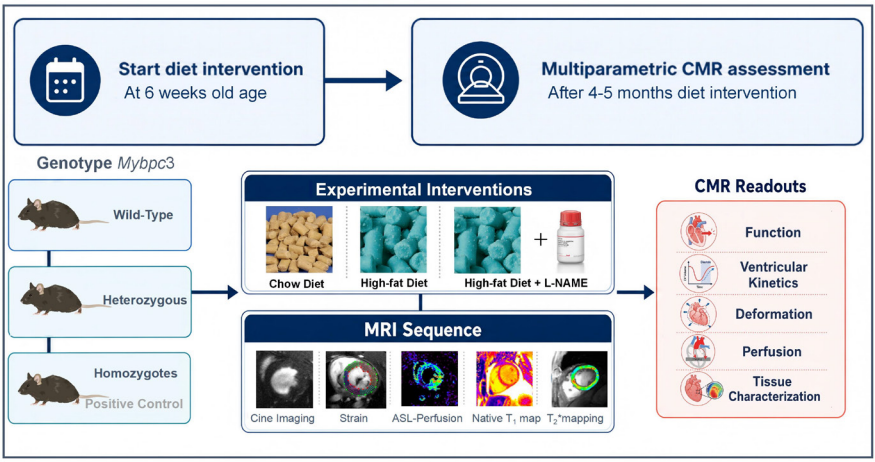

Figure 1. Experimental design and workflow [6]. WT, HET, and KI mice were studied under chow or HFD, with an exploratory HFD plus L-NAME group included to assess additional metabolic and vascular stress. Multiparametric cardiovascular magnetic resonance (CMR) was performed after 4 – 5 months of intervention and integrated cine-derived cardiac function and ventricular kinetics, myocardial deformation, and ASL-based myocardial perfusion. KI mice served as positive controls for the disease phenotype.

Results

HFD induced subtle diastolic and regional MBF abnormalities despite preserved left ventricular ejection fraction (LVEF) and no overt structural remodeling. HFD+L-NAME increased LV mass/EDV in WT and HET mice, while only HET mice showed increases in mean LV wall thickness, global radial strain, and lateral systolic MBF (all $P<0.05$). Lower septal Δ MBF was associated with greater LV mass/EDV in HET chow/HFD mice, while anterior Δ MBF tracked greater global radial strain under HFD ± L-NAME. Both relationships remained after adjustment, whereas associations between filling indices and diastolic radial strain rate were attenuated.

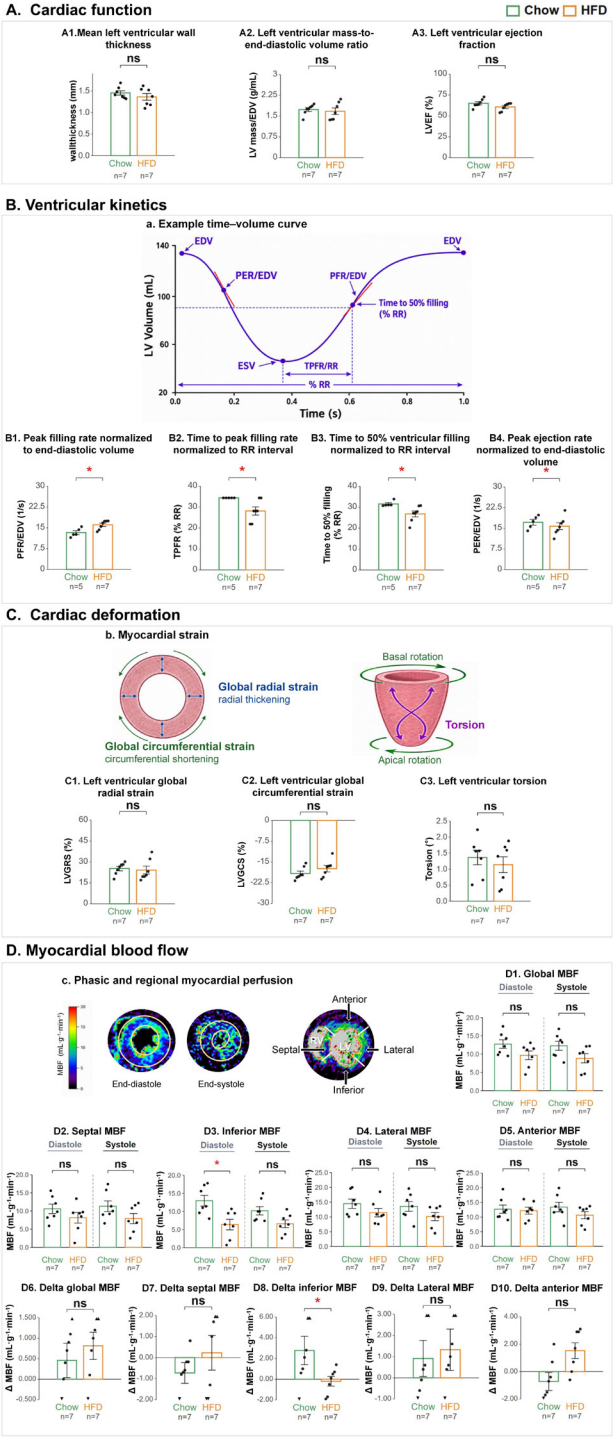
A. Cardiac function
Chow HFD
A1.Mean left ventricular wall thickness
A2. Left ventricular mass-to-end-diastolic volume ratio
A3. Left ventricular ejection fraction
ns
wallthickness (mm)
LV mass/EDV (g/mL)
LVEF (%)
Chow n=7 HFD n=7
B. Ventricular kinetics
a. Example time–volume curve
EDV
PER/EDV
PFR/EDV
Time to 50% filling (% RR)
ESV
TPFR/RR
% RR
LV Volume (mL)
Time (s)
B1. Peak filling rate normalized to end-diastolic volume
B2. Time to peak filling rate normalized to RR interval
B3. Time to 50% ventricular filling normalized to RR interval
B4. Peak ejection rate normalized to end-diastolic volume
PFR/EDV (1/s)
TPFR (% RR)
Time to 50% filling (% RR)
PER/EDV (1/s)
Chow n=5 HFD n=7
C. Cardiac deformation
b. Myocardial strain
Global radial strain
radial thickening
Global circumferential strain
circumferential shortening
Basal rotation
Torsion
Apical rotation
C1. Left ventricular global radial strain
C2. Left ventricular global circumferential strain
C3. Left ventricular torsion
LVGRS (%)
LVGCS (%)
Torsion (°)
D. Myocardial blood flow
c. Phasic and regional myocardial perfusion
MBF (mL·g⁻¹·min⁻¹)
End-diastole
End-systole
Anterior
Septal
Lateral
Inferior
D1. Global MBF
D2. Septal MBF
D3. Inferior MBF
D4. Lateral MBF
D5. Anterior MBF
Diastole
Systole
D6. Delta global MBF
D7. Delta septal MBF
D8. Delta inferior MBF
D9. Delta Lateral MBF
D10. Delta anterior MBF
Δ MBF (mL·g⁻¹·min⁻¹)

Figure 2

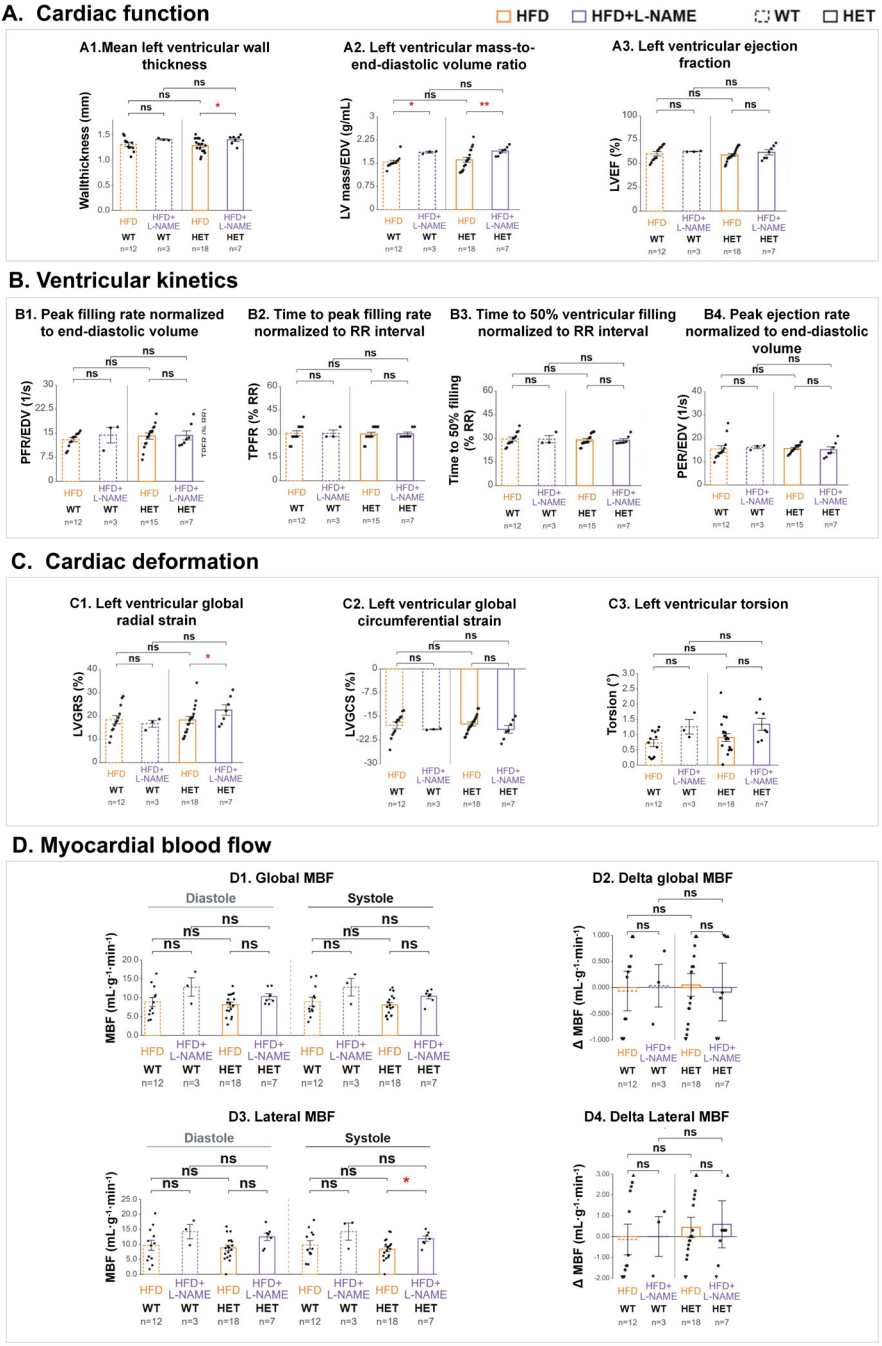
A. Cardiac function
HFD
HFD+L-NAME
WT
HET
A1.Mean left ventricular wall thickness
Wallthickness (mm)
A2. Left ventricular mass-to-end-diastolic volume ratio
LV mass/EDV (g/mL)
A3. Left ventricular ejection fraction
LVEF (%)
B. Ventricular kinetics
B1. Peak filling rate normalized to end-diastolic volume
PFR/EDV (1/s)
B2. Time to peak filling rate normalized to RR interval
TPFR (% RR)
B3. Time to 50% ventricular filling normalized to RR interval
Time to 50% filling (% RR)
B4. Peak ejection rate normalized to end-diastolic volume
PER/EDV (1/s)
C. Cardiac deformation
C1. Left ventricular global radial strain
LVGRS (%)
C2. Left ventricular global circumferential strain
LVGCS (%)
C3. Left ventricular torsion
Torsion (°)
D. Myocardial blood flow
D1. Global MBF
Diastole
Systole
MBF (mL·g-1·min-1)
D2. Delta global MBF
Δ MBF (mL·g-1·min-1)
D3. Lateral MBF
D4. Delta Lateral MBF
ns
n=12
n=3
n=18
n=7
n=15

Figure 3

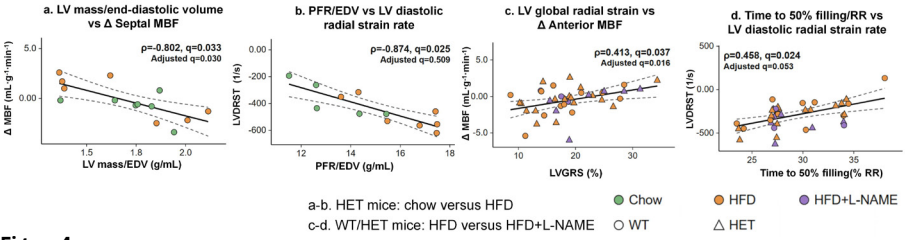

Figure 4

Picture description

Figure 2. High-fat diet reveals early abnormalities in ventricular filling and regional myocardial perfusion in *Mybpc*3-HET mice despite preserved LVEF. Multiparametric CMR findings in *Mybpc*3-HET mice receiving chow or HFD after 4–5 months of intervention. Panels show left ventricular (LV) function and remodeling, quality-controlled time – volume-derived filling and ejection kinetics, myocardial strain and torsion, and phasic and regional ASL-derived myocardial blood flow (MBF) and perfusion reserve (ΔMBF, defined as diastolic minus systolic MBF). HFD induced subtle alterations in filling kinetics and reduced inferior diastolic MBF and ΔMBF despite preserved left ventricular ejection fraction (LVEF) and the absence of overt structural remodeling. Dots represent individual mice and bars indicate mean±SEM. Triangles indicate values outside the displayed y-axis range. *P<0.05; ns, not significant. HC3 robust regression models were adjusted for sex and heart rate where feasible.

Figure 3. Additional L-NAME stress augments cardiac remodeling in HFD-fed mice, with broader structural, mechanical, and perfusion changes in *Mybpc*3-HET mice. Multiparametric CMR comparison of HFD and HFD plus L-NAME in WT and *Mybpc*3-HET mice after 4 – 5 months of intervention. Panels A – C show LV function and remodeling, ventricular kinetics, and myocardial deformation; panel D shows global and lateral phasic MBF and ΔMBF. Addition of L-NAME increased LV mass/end-diastolic volume (EDV) in both WT and HET mice. HET mice additionally showed increased mean LV wall thickness, global radial strain, and lateral systolic MBF, indicating a stronger myocardial phenotype with combined metabolic and vascular stress. Dots represent individual mice and bars indicate mean±SEM. Triangles indicate values outside the displayed y-axis range. *P<0.05; **P<0.01; ns, not significant. HC3 robust regression models were adjusted for sex and heart rate where feasible. Genotype-specific interpretation remains exploratory because of the small WT HFD+L-NAME group.

Figure 4. Regional perfusion reserve (ΔMBF) is associated with LV remodeling, myocardial deformation, and filling abnormalities. Cross-sectional analyses link regional myocardial perfusion abnormalities with structural remodeling and myocardial mechanics. Lower septal ΔMBF was associated with greater LV mass/EDV in *Mybpc*3-HET mice receiving chow or HFD, whereas anterior ΔMBF tracked greater global radial strain under HFD±L-NAME. Both perfusion–remodeling and perfusion–deformation relationships remained after adjustment. Additional analyses relate ventricular filling indices to myocardial deformation, although these associations were attenuated after adjustment. Solid lines indicate unadjusted fits and dashed lines indicate 95% confidence intervals. Labels report Spearman correlation coefficients (ρ) with false discovery rate (FDR)-adjusted q-values and q-values from adjusted regression analyses, where applicable.

Disscussion

These findings support a stress-dependent, spatially heterogeneous phenotype with focal perfusion and filling/mechanical abnormalities despite preserved LVEF. Regional ΔMBF associations with LV mass/EDV and radial strain suggest coupling between microvascular and structural/mechanical remodeling. Serial CMR, T_1/T_2* mapping, and tissue validation will test whether microvascular/tissue changes precede mechanical/structural remodeling.

References

[1] Ho CY, Day SM, Ashley EA, et al. Genotype and lifetime burden of disease in hypertrophic cardiomyopathy. Circulation. 2018;138:1387–1398. doi:10.1161/CIRCULATIONAHA.117.033200.

[2] Ho CY, Carlsen C, Thune JJ, et al. Echocardiographic strain imaging to assess early and late consequences of sarcomere mutations in hypertrophic cardiomyopathy. Circ Cardiovasc Genet. 2009;2:314–321. doi:10.1161/CIRCGENETICS.109.862128.

[3] Nollet EE, Algül S, Goebel M, et al. Western diet triggers cardiac dysfunction in heterozygous *Mybpc*3-targeted knock-in mice: A two-hit model of hypertrophic cardiomyopathy. J Mol Cell Cardiol Plus. 2023;6:100050. doi:10.1016/j.jmccpl.2023.100050.

[4] Schiattarella GG, Altamirano F, Tong D, et al. Nitrosative stress drives heart failure with preserved ejection fraction. Nature. 2019;568:351–356. doi:10.1038/s41586-019-1100-z.

[5] Kober F, Iltis I, Izquierdo M, et al. High-resolution myocardial perfusion mapping in small animals in vivo by spin-labeling gradient-echo imaging. Magn Reson Med. 2004;51:62–67. doi:10.1002/mrm.10676.

[6] Ku MC, Kober F, Lai YC, et al. Cardiovascular magnetic resonance detects microvascular dysfunction in a mouse model of hypertrophic cardiomyopathy. J Cardiovasc Magn Reson. 2021;23:63. doi:10.1186/s12968-021-00754-z.